Development of a compact telescope for cosmic muon flux and density measurements

Sophie Wuyckens

Supervisors : Dr. Andrea Giammanco
Pr. Eduardo Cortina Gil
Examinors : Pr. Giacomo Bruno
Pr. Krzysztof Piotrzkowski

Thesis presented as part of a Master's [120]
in Physics, Research focus

Université catholique de Louvain
Faculté des sciences
Ecole de physique
IRMP/CP3

Academic year 2017-2018

Development of a compact telescope for cosmic muon flux and density measurements

Sophie Wuyckens

Thesis presented as part of a Master's [120] in Physics, in depth-orientation
June 2018

Abstract

Large-area glass Resistive Plate Chambers (gRPC) are widely in use for several High-Energy Physics experiments, and in the context of cosmic-ray muography the TOMUVOL project [1] already demonstrated that this technology is appropriate for volcano studies.

We have developed a muography telescope based on "mini-gRPC" planes based on the same concept as the gRPC detectors used by TOMUVOL and by the CMS [2] and CALICE [3] experiments, but with smaller active area (16x16 cm^2). Its compact size makes it an attractive choice with respect to other detectors previously employed for imaging on similar scales. An important innovation of this design is gas tightness: this makes the detector more "portable" and solves the usual safety and logistic issues for gas detectors operated underground and/or inside small rooms.

This instrument is then designed for challenging operating conditions and could be optimized for applications in geological and archaeological studies as well as for nuclear waste characterization.

Data in real-life operating conditions have been taken at the Mars Desert Research Station (MDRS) in the Utah desert as part of the project UCL to Mars [1] and also at Université catholique de Louvain in the cyclotron building.

In parallel, some geometrical simulations have been performed in order to compare with the real data as well as study the effect on the reconstructed angles due to the misalignement, acceptance and angular resolution of the detectors. Finally a small part was dedicated to the calculation of the signal induced in such a detector.

[1] http://www.ucltomars.org/

Acknowledgments

This masters thesis marks the end of my 5-year academic formation in Physics. I would not be what I am today without the support of many people in my surrounding.

Also, the RPCs telescope project would not have emerged without the help of many people working in the cyclotron building at UCL that were very available all along the year and whom I would like to thank in this preface.

First, I would like to thank my masters thesis supervisors Pr. Eduardo Cortina Gil and Dr. Andrea Giammanco for their support and precious advice in this matter. They spark my interest in experimental particle physics to the highest point. They allowed me to conduct a great study on RPCs while giving me the required tools to do it. I would like to thank also Pr. Giacomo Bruno and Pr. Krzystof Piotrzkowski for having accepted to be the examinors of my master's thesis.

I want to give a special thank to Pavel Demin, one of the computer scientist of CP3, who has designed the data acquisition system but also has helped me in the understanding of the general electronics of the detector. He followed the project since the beginning with very much interest and taught me a lot. I am very grateful for that.

Many thanks to Alexis Fagot and Antoine Pingault from University of Ghent who taught me how to build a resistive plate chamber during my summer internship (August 2018). They have always answered to all of my questions during the whole year and have been available to fill the detectors with their gas system when ours was down.

Next, I'd like to thank Daniel Michotte who has worked on the readout electronics in the electronics lab in the cyclotron building.

Subsequently, I'd like to thank the work of Nicolas Szilasi (mechanical design office) who has designed the profile of the mini-gRPC, as well as the mechanical workshop of the Institut de Recherche en Mathématique et Physique (IRMP) at UCL. They made the pieces for the box and gas valves of the detector described in this user guide.

Many thanks to Jean-Pierre Clare who helped us to restore the gas system but also for having tested the detector tightness several times with its vacuum pump.

Last but not least, a sincere thank to my friends, Adrien Widart, a student in computer sciences, who has helped me a lot with my scripts. Thanks to the *UCL to Mars 2018* crew for their support all along the mission and also to my colleagues in Physics during this two-year masters degree at Université catholique de Louvain.

Contents

Introduction

Discovered by Röntgen in 1895, x-rays allow the study of anatomy in a very precise way in medicine thanks to x-ray photography. Despite the great motivation in the search for the basic properties of the Earth, we know that x-rays are not sufficiently penetrative to successfully target geophysical-scale objects.

In 1936, Carl David Anderson and Seth Neddermeyer discovered the nature of cosmic-ray particles [4] and one of its interaction products with the Earth atmosphere, the muon. Our current knowledge of the muon interaction with matter solves the problem of how to infer the density of inaccessible structures where x-rays (or other conventional imaging techniques) cannot be used. Muography could therefore rise as an alternative.

This technique was first applied for practical purposes in 1955 to measure the overburden over a tunnel [5], and in the late 1960s in a search for hidden chambers in the Second Pyramid of Chephren in Giza [6].

During the last decades, muon imaging has found a multitude of applications in many fields and scientists from accross the globe make advances everyday in detector R&D and data processing making this technology a competitive tool for subsurface imaging of large structures.

For example, since 2006, muography has been used successfully to map the interior of mountains in Japan [7], allowing a finer spatial resolution than what is achievable with conventional geophysics techniques such as gravimetry or seismic tomography. Since then, the technique has been applied to active and dormant volcanoes in other countries, for example Stromboli, Vesuvius and Etna in Italy, Puy de Dôme and La Soufrière de Guadeloupe in France.

Muography is also being applied to surveys of other structures, natural or man-made. In 2015, a muographic image of the nuclear reactor at the Fukushima Dai-ichi nuclear power

plant (damaged by the 2011 Great Tohoku Earthquake and Tsunami) proved that the nuclear meltdown occurred. In 2016 the ScanPyramids mission was able to reach conclusive evidence, through muography, of an unknown cavity in the Great Pyramid of Khufu [8]. In 2017 the MURAVES detector has been used for an archaeological application, mapping the Bourbon Tunnels inside Mt. Echia (Naples, Italy) and providing evidence for a so far unknown room [9].

Various detector technologies have been chosen by different groups, e.g. photographic emulsions, scintillators, and Glass Resistive Plate Chambers (gRPC). In the context of this masters thesis, the mini-gRPCs have been chosen for several reasons : the reduced cost, the compactness, the in-house production and the portability. The project mostly deals with the development of the detector in itself. We started from a simple prototype composed of four planes of mini-gRPCs. This telescope will be further optimized for the investigation of archaeological targets [10] and the remote monitoring of nuclear waste storage [11]. The latter application appears particularly timely considering the reliance on nuclear power of Belgium and other European countries. For these applications, large-area detectors would be impractical, while small telescopes at different locations would allow a complete tomography of the target.

The goal of this thesis is to show how we manage to construct such mini-glass resistive plate chambers and how we could use them to conduct muographic studies.

These devices detect muons therefore in chapter 1, muon physics basics are briefly reviewed as well as the muography techniques that already exist today. Then, the fundamental detector physics of RPCs are described in details in chapter 2. The construction of the mini-gRPCs prototype as well as data collection and analysis obtained are provided in chapter 3. Some geometric simulation tests are explained in chapter 4. Finally, chapter 5 will review the new type of electronics that could further improve the performance of mini-gRPCs.

CHAPTER 1

Aspects of Muon Physics

This chapter cover some particle physics basics needed to understand the properties of muons and more precisely the atmospheric muons that are relevant for the simulations of cosmic ray setups and low-rate muon detectors. An introduction on muography will be elaborated at the end because this is the prime motivation of this project.

1.1 The Standard Model

In the last century, the Standard Model (SM) has been constructed to explain the interactions of the fundamental particles. Scientists conduct experiments everyday such as particle collisions at very high energy to validate it and to understand the properties of these particles.

Despite several experimental proofs of its accuracy, the SM is far from complete. One of its biggest weaknesses is the fact that it does not adequately explain fundamental physical phenomena in nature such as gravitation, dark matter, dark energy, neutrino masses, etc. We still need to reconciliate quantum theory and general relativity in order to get a grand unification of the four interactions. In addition, several theoretical problems cannot be solved such as the hierarchy problem, the strong CP problem, etc.

In the SM, the muon (μ^-) is a fundamental particle and belongs to the lepton family (half-integer spin particle that is not sensitive to strong interaction). It has a mass $m_\mu = 105.6583745\pm$

0.0000024 MeV and a mean lifetime $\tau = 2.1969811 \pm 0.0000022 \times \mu s$ [12] that makes it an unstable particle. It has its corresponding anti-particle with the exact same mass but the opposite charge (μ^+). Just as a side note, the detector described in this thesis is not designed to distinguish them. Thus from now on, the word "muon" will be used to indicate both μ^+ and μ^-.

1.2 Cosmic-rays

1.2.1 History

For a very long time, cosmic rays has been a great mystery. Their effects are known since the 18^{th} century [13]. At that time, scientists were questioning their source: is it from Earth or extra-terrestrial ?

In 1910, the Wulf experiment was conducted on Eiffel Tower [14]. But we had to wait 1912 for two decisive sets of experiment that fixed the existence of cosmic rays. The first was led by Victor Franz Hess who measured the electroscopes discharge with balloons [15] whereas Domenico Pacini made measurements above and under the sea [16].

Many years were still required to understand their composition. Among the pioneers on the subject, we can cite Robert Andrews Millikan with its "Birth cry of atoms" [17], Arthur Compton who measured the latitude effect in 1933 [18] and Alvarez, Compton and Rossi who measured the East-West effect in 1933 [19] [20].

In 1936, Seth H. Neddermeyer and Carl D. Anderson did some important measurements of the energy loss of particles occuring in the cosmic-ray showers and defined the nature of cosmic-ray particles [4]. This episode marks the discovery of muons.

1.2.2 Composition

Today, we know that primary cosmic rays are high energy particles produced in the Universe by solar flares (lowest energy) and by galactic sources like supernovae, pulsars, neutron stars or active galactic nuclei (AGN).

The energy distribution of primary cosmic rays (from a few GeV to $\approx$ 100 TeV) is usually defined by the following power law [21] :

$$I_N(E) \approx 1.8 \times 10^4 \, (E/1\mathrm{GeV})^{-n} \, \frac{\text{nucleons}}{\mathrm{m}^2 \ \mathrm{s} \ \mathrm{sr} \ \mathrm{GeV}} \tag{1.1}$$

where E is the energy per nucleon and $n = 2.7$ is the differential spectral index of the cosmic-ray flux.

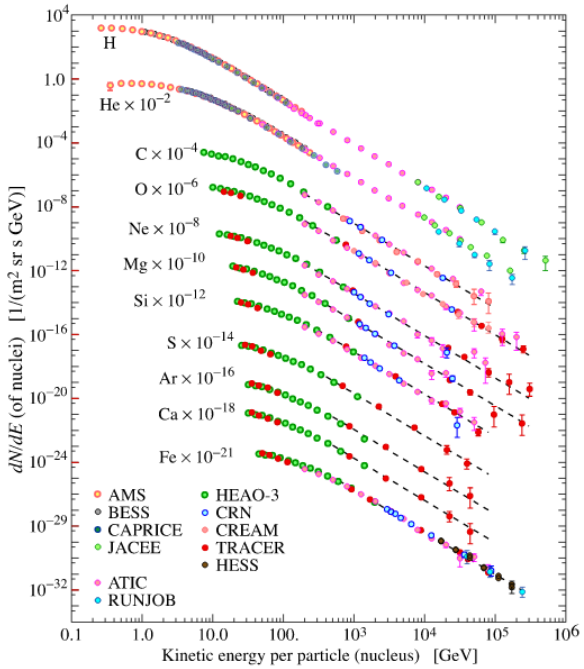

Figure 1.1: Major components of primary cosmic rays [21]

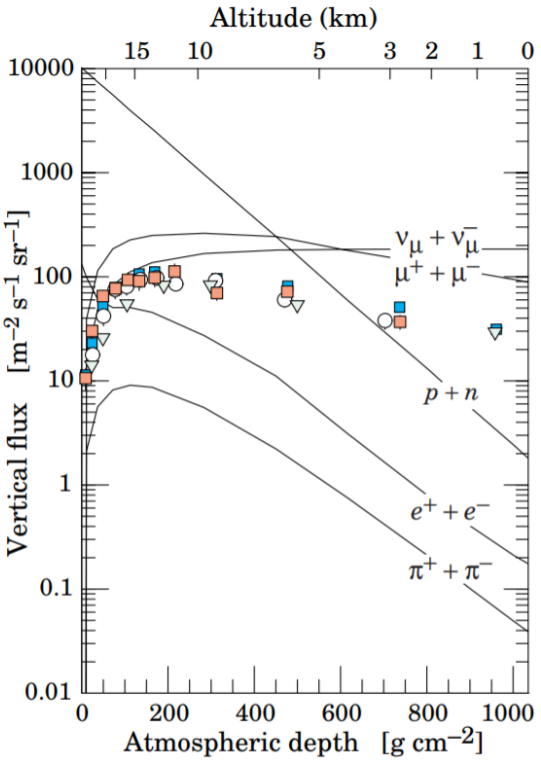

Figure 1.2: Vertical flux of cosmic rays in Earth's atmosphere with $E > 1$ GeV from eq. (1.2) [21]

They are mostly composed by $\sim 90\%$ of protons and $\sim 9\%$ of alpha particles (helium nuclei). Fig. 1.1 shows the composition of primary cosmic rays and their intensity with respect to their kinetic energy.

Today, measurements range up to 3.10^8 TeV.

1.2.3 Showers

When primary cosmic rays reach the Earth's atmosphere, it follows a production of a cascade of reactions with air molecules.

This is called **cosmic shower**. In these reactions in chain, many particles are created such as pions (mostly), kaons, nucleon-antinucleon pairs, etc. (figure 1.2).

The charged pions and kaons are unstable particles and they decay as shown below [22] :

$$BR = (99.98770 \pm 0.00004)\% \qquad \pi \to \mu + \nu_\mu$$
$$BR = (63.56 \pm 0.11)\% \qquad K \to \mu + \nu_\mu$$

The sign was intentionally omitted since we have the decays with positive and negative mesons. Besides, most of the rest of charged kaons decays go to pions as well as neutral kaons which branching ratio is almost 100%. Lastly, the positively charged muons will be more abundant given that the primary cosmic particles are mostly protons which are positively charged.

1.2.4 Atmospheric muons

According to the previous section, atmospheric muons are mainly the product of the collisions of primary cosmic rays with nitrogen and oxygen nuclei at the top of the Earth's atmosphere (10-15 km height).

Due to their unstable character $\boxed{\tau \simeq 2.2\mu s}$, a muon should decay in the atmosphere after $c\tau \cong 660m$ if it has speed of light. However, on fig. 1.2, one notices that muons are the most abundant particles at sea level (easily detectable in contrast to neutrinos). This feature is due to time dilation that allows them to travel longer distances in Earth's atmosphere and reach the sea level.

- Interesting muon features

  Compared to other particles produced in cosmic showers, muons have four major assets :

  1. Larger lifetime compared to other unstable particles, hence most important number of charged particles at sea level.
  2. More massive than electrons : by this property, muons can penetrate through kilometers of rock before interacting unlike electrons that lose all their energy in a few centimeter since their electromagnetic radiation is more important.
  3. No hadronic interactions : they can go deeper than protons and neutrons.
  4. Infinite natural source : no need to produce them with expensive equipment.
  5. Muons are Minimum Ionizing Particles (MIPs) (i.e. particle whose mean energy loss rate through matter is close to the minimum).

  All these features show that muons can be exploited on the Earth's surface.

▶ Energy and angular distribution

The energy distribution of muons is basically the same as the one used for primary cosmic rays that follows a power law E^{-n} (eq. (1.1)) and goes as [23] :

$$I(E) = I_0 N (E_0 + E)^{-n} \left(1 + \frac{E}{\epsilon}\right)^{-1}, \tag{1.2}$$

where,
I_0 : vertical ($\theta = 0$) muon flux integrated over energy
N : normalization constant
E_0 : parameter responsible for energy loss caused by hadronic and electromagnetic interactions with the molecules of the atmosphere (independent of particle energy)
ϵ : parameter accounting for the finite life time of pions and kaons and responsible for high energy behaviour
n : parameter standing for the power of the energy distribution.

From eq. (1.2), the zenith angle distribution of energy integrated flux with $I_0 = \Phi(\theta = 0)$ can be extracted as :

$$\Phi(\theta) = I_0 D(\theta)^{-(n-1)}, \tag{1.3}$$

where $D(\theta)$ corresponds physically to the ratio of pathlengths of a muon from inclined direction to that of a vertical muon and n, the power of the distribution as before.

In the flat earth approximation, $D(\theta) = \frac{1}{cos\theta}$ and eq. (1.3) becomes

$$\Phi(\theta) = I_0 cos^{n-1}\theta. \tag{1.4}$$

One should notice that when $n = 3$, the well-known $cos^2\theta$ angular distribution is obtained however, this expression is only valid at low zenith angle considering the flat Earth approximation.

Gaisser describes the mean muon flux as a function of the muon energy and of the solid angle. Assuming flat Earth, he derived the following formula [24] :

$$\frac{dN_\mu}{dEd\Omega} \approx \frac{1400 E_\mu^{-2.7}}{m^2\ s\ sr\ GeV} \times \left(\frac{1}{1 + \frac{1.1 \times Ecos\theta}{\epsilon_\pi}} + \frac{0.054}{1 + \frac{1.1 \times Ecos\theta}{\epsilon_K}}\right), \tag{1.5}$$

where $\epsilon_\pi \approx 115$ GeV and $\epsilon_K > 850$ GeV give the contributions of pions and kaons.

Fig. 1.3a and 1.3b show examples of data sets at two different zenith angles. The data are fitted with eq. (1.2) and the Gaisser distribution eq. (1.5). Eq (1.2) gives an excellent fit whereas Gaisser fit seems to be valid only at high energy momentum.

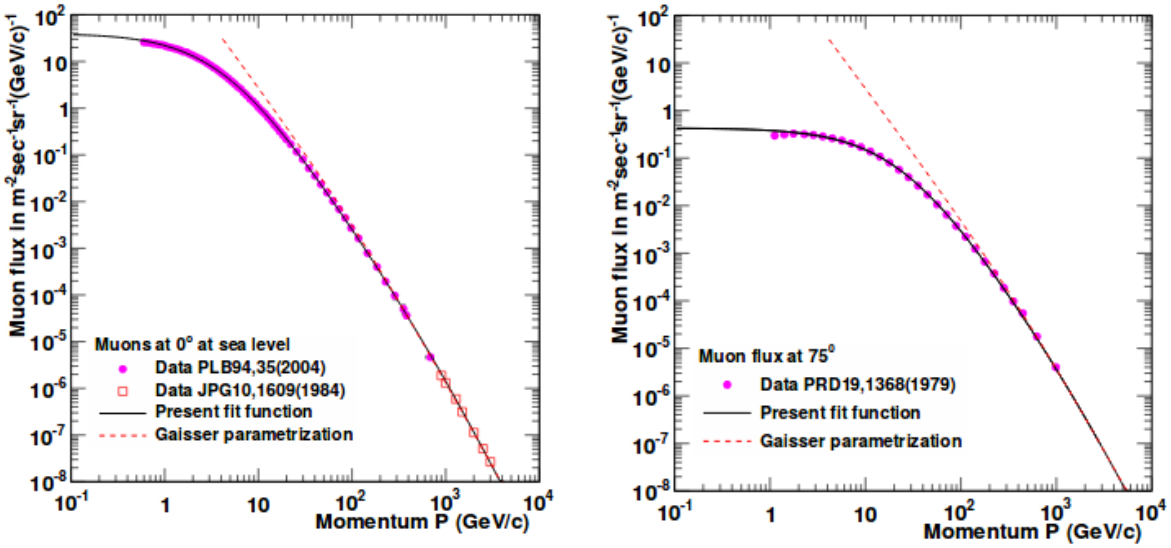

(a) $\theta = 0°$ (b) $\theta = 75°$

Figure 1.3: Muon flux at two different zenith angles at sea level [23]

The fit parameters of these two data sets are listed in table 3.1. The larger the zenith angle, the lower the integrated flux I_0. The parameter E_0 will increase because the muon pathlength will be longer at inclined angles.

Table 1.1: Fit parameters of muon energy distributions of fig. 1.3a and 1.3b

	I_0 $(m^{-2}$ $s^{-1}sr^{-1})$	n	E_0 (GeV)	$1/\epsilon$ $(GeV)^{-1}$
$\theta = 0°$	88.50 ± 0.25	3.00 ± 0.04	4.28 ± 0.05	1/854
$\theta = 75°$	71 ± 2	3.00 ± 0.02	23.78 ± 0.30	1/2000

By fitting the parameters (table 1.2) of eq. (1.3) and (1.4), we obtain the muon flux as a function of the zenith angle. This is shown in fig. 1.4.

Table 1.2: Fit parameters of muon zenith angle distributions of fig. 1.4

	I_0 $(m^{-2}$ $s^{-1}sr^{-1})$	n	χ^2/ndf
Eq. 1.3	88.0 ± 2.4	3.09 ± 0.03	111/37
Eq. 1.4	85.6 ± 22.4	3.01 ± 0.01	52/17

Eq. (1.3) is an excellent function to fit the data at all zenith angles given the result of the χ^2 test. In addition, table 1.2 demonstrates that the fitted parameters I_0 and n match very well with the ones obtained in table 1.1.

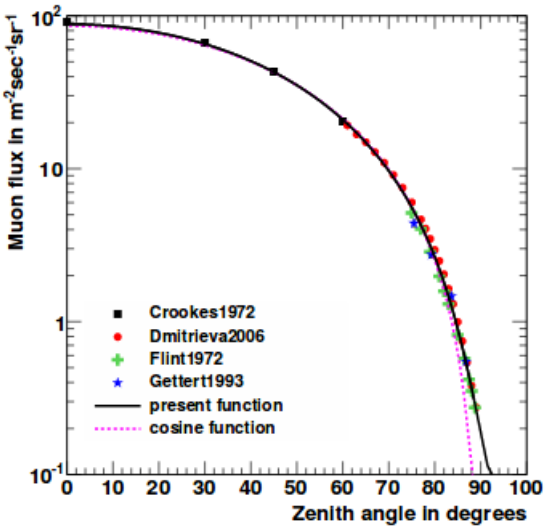

Figure 1.4: Zenith angle distribution at sea level fitted with eq. (1.3) and (1.4) [23]

These studies show the analytical functions proposed to describe muon angle and energy distribution. They use a modified power law for this purpose. Since the detector developped in this thesis has as primary goal the study of the muon flux as a function of the zenith angle, we would expect to get the same form as in fig. 1.4 and thus a parameter n close to 3. The muon momentum distribution will not be established given that our technology does not allow to record the energy of the crossing muon.

- Muons rate

As a general rule, we say that the Earth is continuously bombarded by muons at a rate of 1000 particles/m² sec at the top of the Earth's atmosphere [25] or equivalently one muon per minute per thumb nail. Their mean energy is around 4 GeV and their angular distribution should be close to $cos^2\theta$ (eq 1.4).

However, the **muons rate** vary because of several factors [26]:

- Latitude effect : There are more muons at the poles due to the magnetic field that surrounds and protects the Earth.
- Solar activity : When the Sun is highly active, there are less muons because the magnetic field of the Sun seems to leave out lower cosmic ray particles. The flux is then anti-correlated with the Sun's cycle of 11 years.
- Upper atmospheric temperature : There are more muons in summer because the atmosphere temperature is higher which results in a increase of the mean free path of pions and kaons (and their probability to decay into muons).
- Atmospheric pressure : There are more muons when the pressure is lower. If the quantity of air is reduced, it will absorb less muons.

1.3 Interactions of muons with matter

If we want to detect something, we have to make it interact with matter. Understanding and proper use of any kind of detector requires to understand the fundamental mechanisms of different radiation interactions with the active materials.

The passage of heavy charged particles like muons through matter can be caracterized by two features. On one side, we have the loss of energy by the particle and on the other side we have the deflection of the particle from its incident direction.

The processes that can generate such effects are mainly due to inelastic collisions with atomic electrons. We use to subdivide these processes in two categories : the soft collisions (i.e. excitation of the atoms) and the hard collisions (i.e. ionization of the atoms) [27].

- Energy loss

  By using a probabilistic approach, we define the mean energy loss per unit of lenth traversed or **stopping power (S)**. It can be described by the Bethe-Bloch formula [28]. However, this formula is only valid for a specific range of the incoming particle energy.

  In general, in order to describe the mean stopping power of muons, we use the following formula [29]:

$$\left\langle -\frac{dE}{dx} \right\rangle = a(E) + b(E)E, \tag{1.6}$$

  with,
  $a(E)$: Stopping power due to ionization energy loss (electronic processes)
  $b(E)$: Stopping power due to radiative processes (bremsstralung, direct production of e^+e^- pairs, and photonuclear interactions).

  As an example, some calculations are given below.

  a) 4 GeV-muon range in rock

  With $a_{rock} \simeq 2$ MeV/(g/cm²) and $b_{rock} \simeq 4.4 \cdot 10^{-6}$ (g/cm²)$^{-1}$, we have :

$$\begin{aligned} \hat{\text{R}}(\text{E}) &= \int_E^0 \frac{dE}{(\frac{-dE}{dx})} = \frac{1}{b} ln(1 + \frac{b}{a}E)\Big|_{4GeV}^0 \\ &= 1991.25 g/cm^2 \end{aligned}$$

  As $\rho_{rock} = 2.65 \text{gcm}^{-3}$ [PDG], $\Rightarrow \text{R(E)} = \frac{\hat{\text{R}}(\text{E})}{\rho} \simeq 751.42cm \sim \boxed{7m}$

  This result confirms the high penetrating power of muons.

b) Signal expected in parallel plate chambers with a gap of $\Delta x =$**1mm** filled with **argon** if a muon passes through the detector (at 1 atm and 20°C)

Useful data : $\rho_{Ar} = 1.662 \cdot 10^{-3}$ g/cm^3, $\quad \left\langle -\frac{dE}{dx} \right\rangle_{min} = 1.519$ MeV cm²/g.

As a general rule, the number of primary ion pairs produced is defined by $N = \frac{\Delta E}{w}$ where ΔE is the deposited energy and w is the average energy to produce an ion pair.

Here, $w_{Ar} = 26.4$ eV/ion-pair [27]. Therefore, we have :

$$\Delta E = \Delta x \cdot \rho_{Ar} \cdot \left\langle -\frac{dE}{dx} \right\rangle_{min} \approx 252.46eV$$
$$Q_{dep} = Ne = \frac{\Delta E}{w} e = \boxed{1.53 \cdot 10^{-18} C}$$

While the measured charge is calculted with :

$$Q_{meas} = \int \frac{V}{R} dt, \tag{1.7}$$

where V is the amplitude of the signal and R, the resistance of the front-end board.

If we use the sample obtained with the oscilloscope (with a termination of $R = 50\Omega$) that is showed in chapter 3 fig. 3.16, time is discretised and the integral becomes a sum as follows :

$$Q_{meas} = \frac{1}{R} \sum_i V_i \Delta t$$

The time width of this signal being $\Delta t = 14$ ns, we finally obtain : $\boxed{Q_{meas} = 1.15 \cdot 10^{-11} C}$.

The multiplication factor is then $\boxed{M = \frac{Q_{meas}}{Q_{dep}} \sim 10^7}$.

As you can see, the signal is still very small. Amplifiers are needed for this type of gas detector.

▶ Multiple scattering processes

We talked about energy loss due to scattering with electrons but scatterings with nuclei also generate deflections of the incident charged particle trajectory, the "multiple scattering". The deviations themselves are not large but their number is important.

To describe multiple scattring angles, a distribution derived from Moliere's theory is used. Small scattering angles are normally distributed around $\Theta = 0$ whereas large scattering angles are more frequent than expected from Gaussian distribution.

We define the standard deviation θ_0 as [27] :

$$\left\langle \Theta^2 \right\rangle = \left\langle \Theta_\theta^2 \right\rangle + \left\langle \Theta_\phi^2 \right\rangle ; \tag{1.8}$$

$$\theta_0 = \sqrt{\langle \Theta^2 \rangle} = \frac{13.6\text{MeV}}{\beta pc} z \sqrt{\frac{x}{X_0}} \left[1 + 0.038 ln(x/X_0)\right] ; \tag{1.9}$$

where p is the momentum and X_0 is the radiation length (characteristic of the material) approximated by the following formula :

$$X_0 = \frac{716.4 \cdot A}{Z(Z+1) ln(\frac{287}{\sqrt{Z}})} \text{g/cm}^2. \tag{1.10}$$

For example, in a block or layer 10 cm thick, a 3-GeV muon would scatter with a mean angle of 2.5 mrad in water ($X_0 = 36.08\text{g} \cdot \text{cm}^{-2}$), 11 mrad in iron ($X_0 = 13.84\text{g} \cdot \text{cm}^{-2}$), and 25 mrad in tungsten ($X_0 = 6.76\text{g} \cdot \text{cm}^{-2}$)[1]. The inverse operation can also be done to find the thickness of the target if we measure the muon scattering angle and know its momentum.

1.4 Muography

Absorption and/or Coulomb scattering of charged muons described in the previous section can be used to image matter, this is called **muography**. The basic concept consists in using the attenuation or deviation of muons to image large and/or dense objects where conventional techniques cannot work.

In general, muography techniques are divided into two categories : **Deviation** (thin and small objects) and **transmission** (or absorption) (large and thick objects). In the next paragraphs, we elaborate on each one.

- Absorption radiography

  This technique measures the incoming muon flux to produce images of objects (fig. 1.5 & fig. 1.7). It is based on the fact that muons lose energy according to eq. 1.6 when they pass through an object and only a fraction of them survive. But this fraction can also be determined by the object opacity that is defined by the integrated density over the path length $\int \rho dx$.

  Therefore, experimentally, we measure this fraction in different directions through the target and then reconstruct the average opacity map of it, integrated along these directions. And if in addition, we know the target thickness, a density cartography can be established.

[1] `http://pdg.lbl.gov/2017/AtomicNuclearProperties/index.html`

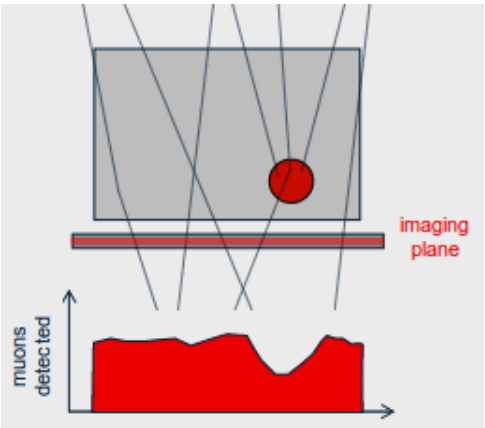

Figure 1.5: Absorption radiography [30]

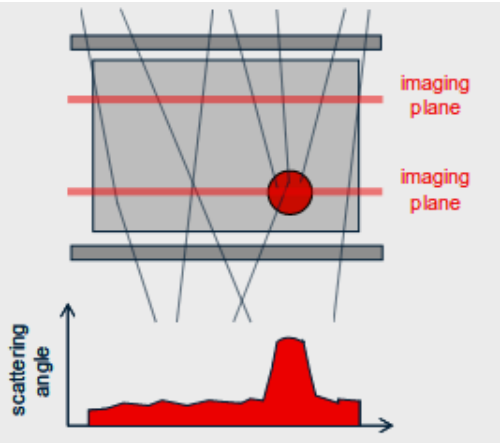

Figure 1.6: Tomography with deviation [30]

However, it is rather slow (from days to months) because we need many muon tracks to obtain a good image. Multiple scattering existing in the target and between the target and the detector are the reasons for this low-speed muon-imaging. It decreases the angular resolution.

Absorption muography can be subdivided into two categories [26] :

Single measurement : It provides 2D images and projected average density maps thanks to eq 1.6.

Multiple measurements (from different detector's installation points) : It provides 3D density maps. We can also do triangulation to localize objects.

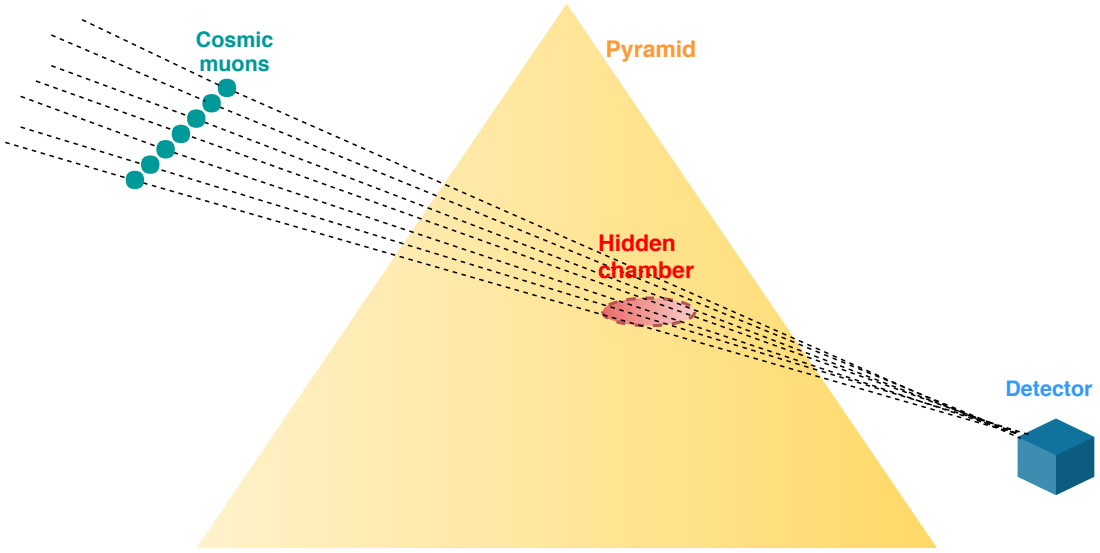

Figure 1.7: Example of absorption radiography application : Pyramid

- Scattering tomography

  If we reconstruct diffusion centers of muons, 3D imaging can be realized (fig. 1.6 & fig 1.8). Indeed, the study of the deviation angle θ_0 of muons giving by eq. 1.8 as a function of the 3D position within the object allows us by inversion to provide 3D density map as for muon absorption and to some extent determine the material of objects traversed by muons (sensitivity to its atomic weight).

  The detector configuration has to surround the target in order to reconstruct upstream and downstream muon trajectories.

  Deviation tomography has the advantage to be fast (from minutes to days) compared to transmission muography because we collect and use more information. However, each scale has its preferred technique and for example, the deviation mode is not adapted when opacity is too large given that multiple scattering occur more often ant it makes more difficult to reconstruct the point where the muon scatters in the medium.

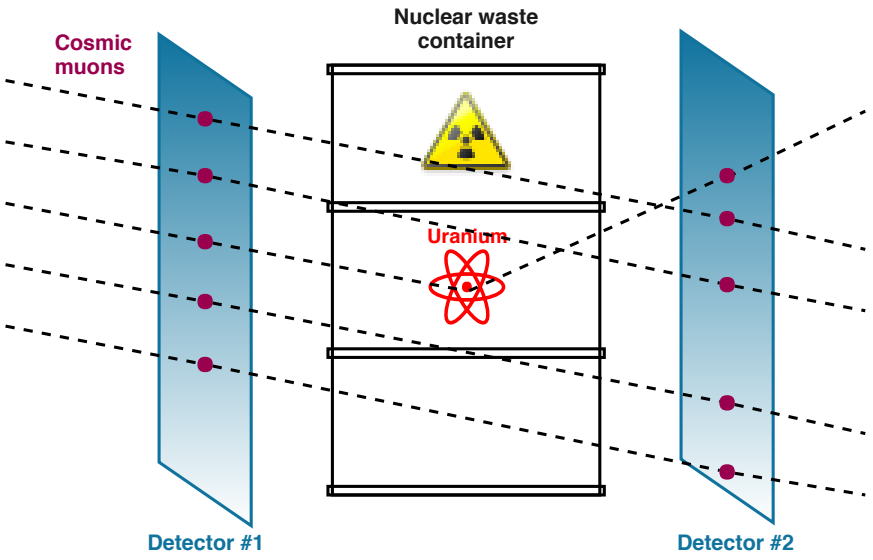

Figure 1.8: Example of deviation tomography application : Nuclear waste characterization

Today, muography applications are on the rise. Among the most-known, there are : volcanology, archeology, civil engineering, nuclear reactor monitoring, nuclear waste characterization, underground mapping, CO_2/fuel geological storage and monitoring, etc.

To conduct such experiments, muon imaging technologies require specific features (sometimes contradictory) :

- Excellent angular resolution to obtain reliable and accurate imaging
- Large acceptance to cover large structures

- Robustness to operate sometimes in harsh conditions. Variations of temperature and pressure could lead to density variations of material that affect the gain. The stability is then very important.
- Autonomy : electrical consumption has to be as low as possible or not present
- Cost : the cheaper the better

Three types of detector technologies are generally used: (a) scintillators, (b) nuclear emulsion, and (c) gaseous detectors. Their main features are listed in table 1.3.

Table 1.3: Main characteristics of most-used muon imaging technologies [26]

	Major asset	Spatial resolution	Direct imaging	Sensitivity to environmental conditions	(Electric) consumption	Common use in muography
(a)	robustness	$\sim$1 cm	y	n	low	Volcanoes Homeland security
(b)	precision	$< 1\mu$m	n	y at high T (°C)	n	Volcanoes Archeology
(c)	versatility	$\sim 0.1 - 1mm$	y	y (gain depends on T and P)	low + gas	Volcanoes Homeland security Archeology

In the context of this masters thesis, a gas detector has been chosen. Gas detectors include numerous advantages like their resolution with a few hundred of microns (versus scintillators, factor of 10 better !), their cost and their direct imaging (versus nuclear emulsions) that allows dynamical studies.

In conclusion, this chapter allowed us to become more familiar with relevant subjects for the topic studied i.e. the origin and properties of cosmic muons as well as their mechanisms of interaction with matter that can be exploited in order to conduct muographic studies.

Now, let's elaborate on the type of instrument chosen to detect the muons : resistive plate chambers.

CHAPTER 2

Resistive plate chambers

In this chapter, we review the main properties of resistive plate chambers.

Developed in 1981 by R. Santonico and R. Cardarelli [31], Resistive Plate Chambers (RPCs) are gaseous detectors that consist of two parallel plate electrodes of high resistivity that act as a capacitor. RPCs are known through the world of experimental particle physics because they are used for detecting muons in several modern particle physics experiments including ATLAS [32], CMS [2], and BES III [33]. They combine a good spatial resolution with a time resolution of just one nanosecond but have also a high efficiency and a reduced cost.

2.1 Working principle

Fig. 2.1 gives a schematic view of an resistive plate chamber detector. On the outside of these resistive plates a conductive coating is applied. By connecting one of these coatings to a high voltage (HV) source and grounding the other coating, the resistive plates become a cathode and an anode respectively. This results in an electric field inside the gap between the electrodes filled with gas.

When an energetic charged particle, e.g. a muon, passes accross the detector and ionizes the gas molecules, it leaves an ionising track according to the Bethe-Bloch formula for the work-

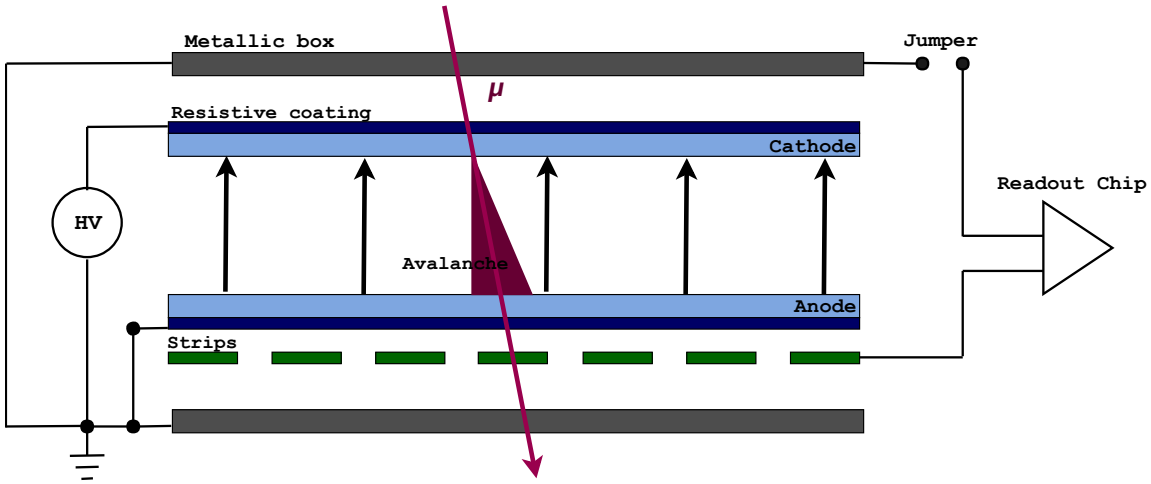

Figure 2.1: Simple view of the working principle of a RPC.

ing gas as discussed in section 1.3. This liberates free electrons and ions which are accelerated by the strong electric field towards the anode and the cathode respectively. When the electric field is higher than a threshold value, primary electrons originated from ionization acquire sufficient energy between collisions to produce new ionizations. Secondary electrons can produce tertiary ones and an avalanche begins. This phenomenon is called a *Townsend avalanche*, i.e. on average every colliding electron liberates more electrons and an exponential growth of the number of free electrons occurs. The signal is then induced on the read-out strips [34].

In these conditions, the number of ion pairs per unit path length is proportional to the total number of ion pairs initially generated [35].

Let Q be the total charge generated by the avalanche process, we have :

$$Q = n_0 e M, \tag{2.1}$$

where,
n_0 : number of original ion pairs created
M : Multiplication factor

The Townsend equation gives the fractional increase in the number of charged pairs per unit length :

$$\frac{dN}{dx} = \alpha N \Rightarrow N(x) = N_0 e^{\alpha x}, \tag{2.2}$$

where,
N_0 : number of primary ion-pairs
α : First Townsend coefficient which stands for the number of collisions leading to ionization per unit length of the particle track.
x : Distance from the anode.

This avalanche process is a key part of the particle detection by means of a RPC.

The reason we use resistive plates instead of metallic ones is due to the fact that we do not want the signal to spread over the entire electrode. We want a local signal induced on the strips to obtain a good spatial resolution. The spot where the avalanche reaches the electrode is slowly recharged by a small current flowing through the electrode.

The avalanche mode of an RPC can work only if the electric field is sufficiently strong otherwise, the signal will be too small and we would detect nothing (drift-only regime). In another way, a RPC can be operated in the streamer mode (or spark mode). This regime can be reached if the electric field is increased beyond the avalanche mode. The charge generated on the electrodes is bigger (almost 100 times higher - fig. 2.2) but in return the recharge time lasts longer. Therefore, there is a more important dead time in this regime and it leads to a rate limitation that can be visualized in fig. 2.3.

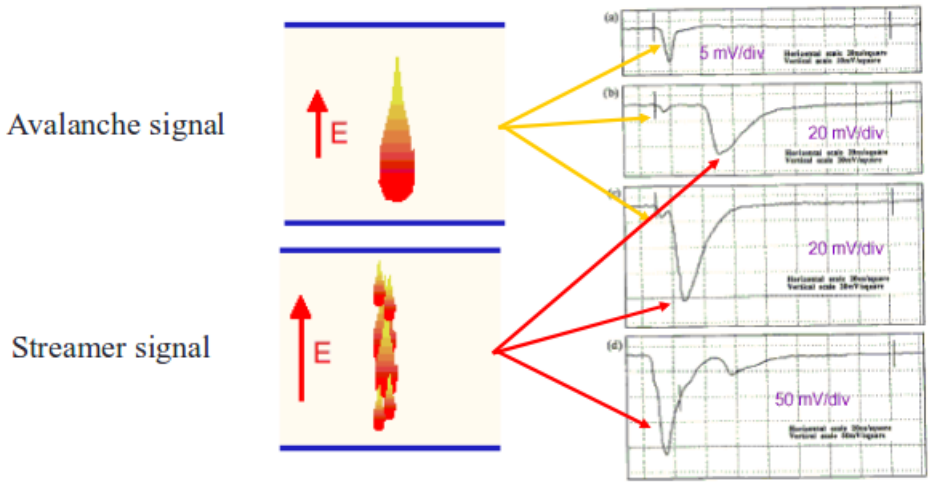

Figure 2.2: Streamer versus avalanche mode (pictures taken from Imad Laktineh's lectures [36]) [37]

2.2 Signal formation

The mechanism of signal formation in RPC is very simple and is applied in most gas-filled ion chambers, proportional counters and even in semi conductor detectors. Signals from detectors arise because of the motion of charge carriers after they are formed by the incident radiation.

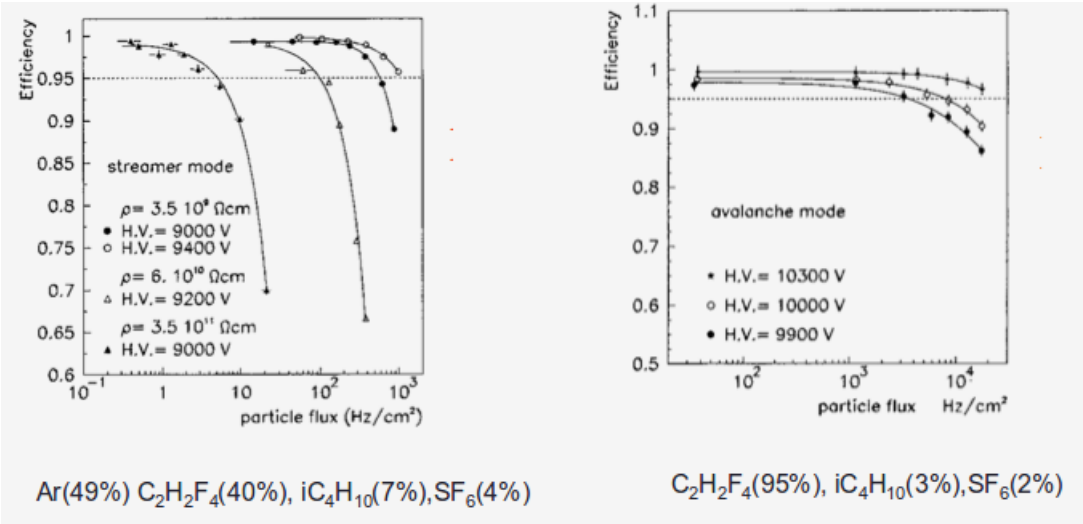

Figure 2.3: Study of the efficiency of RPCs versus the particle flux in two cases. Left figure : Streamer mode. Right figure : Avalanche mode. [36]

2.2.1 Shockley-Ramo theorem

Usually, to estimate the signal on perfectly **conducting** electrodes wrapped by insulating material, we look at induced charge or instantaneous current on electrodes. The signal arises from the motion of charge carriers in a detector and it can be calculated thanks to the Shockley-Ramo Theorem [38] and the concepts of the weighting field and weighting potential. This theorem states that the instantaneous current induced on a metallic electrode is given by:

$$i(t) = q\vec{v}(t) \cdot \vec{E}_w(\vec{x}(t)), \tag{2.3}$$

where q is the charge of the carrier (electron/ion), $\vec{v}$ is its velocity, and $\vec{E}_w$ is called the weighting field that exists in the detector in the absence of the charge and when the electrode (that we look at for a signal) is put to unit voltage while the others are grounded (fig. 2.4). The demonstration is given in appendix 1.

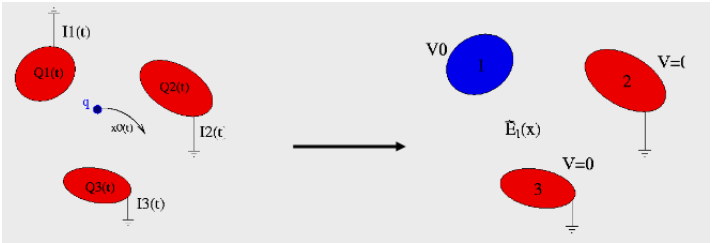

Figure 2.4: Ramo's theorem visualization and concept of weighting field. It allows to calculate the current induced on a grounded electrode by a charge q moving along a trajectory $x_0(t)$.

In the case of an ionization chamber with a parallel plate geometry, this theorem gives a result immediately if we consider that the velocity equals to $\vec{v} = \mu\vec{E}$ where μ is the mobility (different

for electrons and ions). $\vec{E}$ is then the actual field of the detector ($= \frac{V}{d}$) whereas the weighting field equals $\vec{E}_w = \frac{1}{d}$. We find,

$$i = q\frac{\mu V}{d^2}. \tag{2.4}$$

This equation is only a rough approximation in case of segmented electrodes. For a more specific configuration of a detector, we can calculate the weighting potential/field if we solve the Laplace equation :

$$E_w = -\nabla V_1. \tag{2.5}$$

In order to take into account the avalanche process in the calculated induced current and charge, one has only to convolute the mean induced current with the charge produced in the avalanche in the following way [39] :

$$i(x,t) = \frac{E_w}{V_w} e_0 v_D e^{(\alpha-\beta)v_D t} \Theta\left(\frac{d-x}{v_D} - t\right); \tag{2.6}$$

$$Q_{ind}(d-x) = \int_0^t i(x,t)dt = \left[\frac{E_w}{V_w(\alpha-\beta)}\right] e_0(e^{(\alpha-\beta)(d-x)} - 1); \tag{2.7}$$

where ,
$\Theta(x)$: step function indicating when the electrons reach the anode i.e. when the current suddenly stopped.
α : first Townsend coefficient
β : attachement coefficient
e_0 : electron charge
E_w : weighting field

2.2.2 Shockley-Ramo theorem extension

Eq. (2.3) is only valid if the electrodes are perfect conductors surrounded by insulating materials that produce instantaneous currents. In our case, as its name suggests, RPC contain resistive elements, hence we cannot use Ramo theorem as it was presented in section 2.2.1. We have to take into account not only the time dependence of the signals given by the movement of the charge density $\rho(\vec{x},t)$ but also the time-dependent reaction of the medium with arbitrary conductivity $\sigma(\vec{x},s)$ and permittivity $\epsilon(\vec{x},s)$.

To deal with that, W. Riegler extended the Ramo theorem [40] [41]. Working with the quasistatic approximation of Maxwell's equation in Laplace domain, he suggested to absorb the conductivity in the definition of the permealibility (by replacing $\epsilon(\vec{r},s)$ with $\epsilon(\vec{r},s)+\frac{1}{s}\sigma(\vec{r},s)$). Demonstration is shown in appendix 2. Its general results can be written as follows :

$$V_1(t) = \frac{1}{q_0}\int_0^t \int_V \Psi_V(\vec{x'}, t-t')\frac{\partial \rho_e(\vec{x'}, t')}{\partial t'} d^3x' dt'; \tag{2.8}$$

$$I_1^G(t) = \frac{1}{v_0}\int_0^t \int_V \Psi_I(\vec{x'}, t-t')\frac{\partial \rho_e(\vec{x'}, t')}{\partial t'} d^3x' dt'. \tag{2.9}$$

Eq. (2.8) gives the induced voltage on electrode 1 by a time-dependant charge distribution $\rho_e(\vec{x}, t)$ placed in a medium with a permittivity $\epsilon(\vec{x}, s)$ and conductivity $\sigma(\vec{x}, s)$. It is calculated by removing the charge and applying a delta current $q_0\delta(t)$ on electrode 1 which results in a time-dependent potential $\Psi_V(\vec{x}, t)$, called the weighting potential between the electrodes that can be easily computed.

Whereas Eq.(2.9) gives the induced current on the grounded electrode 1 by a time-dependant charge distribution $\rho_e(\vec{x}, t)$ placed in a medium with a permittivity $\epsilon(\vec{x}, s)$ and conductivity $\sigma(\vec{x}, s)$. It is calculated by removing the charge and applying a delta voltage pulse $v_0\delta(t)$ on electrode 1 which results in a time-dependent potential $\Psi_I(\vec{x}, t)$, called the weighting potential between the electrodes that can be easily computed.

If now we take into account that the charge is **moving** and consists of an **ion-pair**, we should write the charge density as follows :

$$\begin{aligned} \rho_e(\vec{x}, t) &= \Theta\left[Q\delta^3(\vec{x} - \vec{x_1}(t)) - Q\delta^3(\vec{x} - \vec{x_2}(t))\right]; \\ \vec{x_1}(t=0) &= \vec{x_2}(t=0); \end{aligned}$$

where $\vec{x_1}(t)$ & $\vec{x_2}(t)$ stand for the trajectory and speed of the electron and ion.

Hence with $\vec{E}_V(\vec{x}, t) = -\vec{\nabla}\Psi_V(\vec{x}, t)$, eq. (2.6) and (2.7) become :

$$\begin{aligned} V_1(t) &= \frac{Q}{q_0}\int_0^t \vec{E_V}(\vec{x_1}(t'), t-t')\vec{v_1}(t')dt' + \frac{Q}{q_0}\int_0^t \vec{E_V}(\vec{x_2}(t'), t-t')\vec{v_2}(t')dt'; \\ I_1(t) &= \frac{Q}{v_0}\int_0^t \vec{E_I}(\vec{x_1}(t'), t-t')\vec{v_1}(t')dt' + \frac{Q}{v_0}\int_0^t \vec{E_I}(\vec{x_2}(t'), t-t')\vec{v_2}(t')dt'. \end{aligned}$$

Application of the Ramo theorem to signals in RPC.

We want to find the induced current in electrode 1 by a moving charge Q between two resistive layers defined as :

$$I_1(t) = \frac{Q}{V_0} \int_0^t \vec{E}_1 \left[\vec{x}(t'), t - t'\right] \vec{v}(t') dt', \tag{2.10}$$

where $\vec{E_1}$ the weighting field and $x(\vec{t})$ the charge trajectory.

At first sight, this equation looks very similar to basic Ramo theorem. In fact, the difficulty here resides in the calculation of the weighting field which now depends on time.

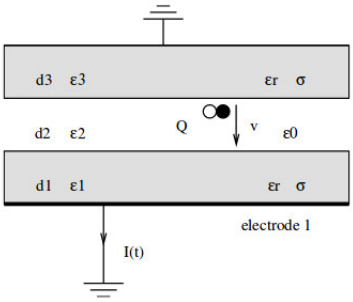

Figure 2.5: Ramo theorem extended. The charge moving in the gas gap induces a current on the infinite planar electrode 1 with finite resistivity.

The case of an infinite planar electrode is chosen for the sake of simplicity. Moreover, in most of the cases, it is quite close to reality, in particular for our RPCs.

First we want calculate the electrostatic weighting field of electrode 1 (put at voltage v_0) in the gas gap:

$$E_z = E_2 = \frac{v_0 \epsilon_1 \epsilon_3}{\epsilon_2 \epsilon_3 d_2 + \epsilon_1 \epsilon_3 d_1 + \epsilon_1 \epsilon_2 d_3)}, \tag{2.11}$$

with $\epsilon_1 = \epsilon_3 = \epsilon_0 \epsilon_r$ and $\epsilon_2 = \epsilon_0$, we just have to apply the statements of W. Riegler's theorems by replacing $\epsilon_1, \epsilon_3 \to \epsilon_0 \epsilon_r + \frac{1}{s}\sigma$ and then we get,

$$E_z = \frac{(\sigma + \epsilon_0 \epsilon_r s) v_0}{(\sigma + \epsilon_0 \epsilon_r s) d_2 + \epsilon_0 (d_1 + d_3) s}; \tag{2.12}$$

$$E_z(t) = v_0 \left(\frac{\epsilon_r}{d_1 + d_3 + \epsilon_r d_2} \delta(t) + \frac{\sigma}{\epsilon_0} \frac{d_1 + d_3}{(d_1 + d_3 + \epsilon_r d_2)^2} e^{-t/\tau} \right); \tag{2.13}$$

where $\tau = \frac{\epsilon_0}{\sigma} \frac{d_1 + d_3 + \epsilon_r d_2}{d_2}$ and the second eq. (2.13) being the inverse Laplace transform.

By using eq. (2.10), the current induced by a charge Q created at t=0 with a velocity v moving accross the gas gap to reach the resistive layer at $T = d_2/v$ is then given by :

$$t < T \qquad I(t) = \frac{Qv}{(d_1 + d_3 + \epsilon_r d_2)} \left[\epsilon_r + \frac{d_1 + d_3}{d_2}(1 - e^{-t/\tau}) \right]; \tag{2.14}$$

$$t > T \qquad I(t) = \frac{Qv}{(d_1 + d_3 + \epsilon_r d_2)} \left[\frac{d_1 + d_3}{d_2}(e^{T/\tau} - 1)e^{-t/\tau} \right]. \tag{2.15}$$

In the case of a strips geometry, the weighting field is much more complicated to compute since we cannot derive the potential with an analytical expression. It requires superpositions of particular solutions of the homogeneous potential equation that can be infinite series or integrals [42].

2.3 Electrode materials

To ensure a good rate capability (R), the resistive plate material has to be chosen carefully ($R \propto \frac{1}{\rho \times t}$ with t, the thickness and ρ, the resistivity) [43]. If the bulk resistivity is too low, the spatial resolution is reduced because the signal would spread accross the plate. If the resistivity is rather high, the electrodes will take a larger time to recharge which is not convenient for high rate events [44] [34].

From the section 2.2, we also know that the permittivity and resistivity of the gas gap and of the plates play an important role for the uniformity of the electric field accross the detector.

The resistivity of a material for RPC should remain stable because otherwise it would affect the rate capability. This problem is in fact a consequence of the ageing of a detector and it affects a lot bakelite-based RPCs (see fig. 2.6 (b) & (c)). The reason comes from macroscopic conduction process in bakelite. Given that the conduction process is led by the H^+ ions, when the detector is ageing water evaporation appears and these ions are not there anymore to form the current flow. As a result, the resistivity of the electrode rises and the detector has some trouble to recharge [45]. People try to avoid this problem by adding vapour to the gas mixture and maintain humidity and it seems to work (see fig. 2.6 (a)).

The most used materials are listed in table 2.1 with their pros and cons.

2.4 Resistive coating

A resistive coating is applied on the outside of the plates in RPCs configuration in order to uniformly distribute the high voltage and produce a uniform electric field and ensure that the gas gap can easily recharge after an ionizing event [47]. We just have to be careful not to shield the readout strips too much from the charges moving inside the gap [48].

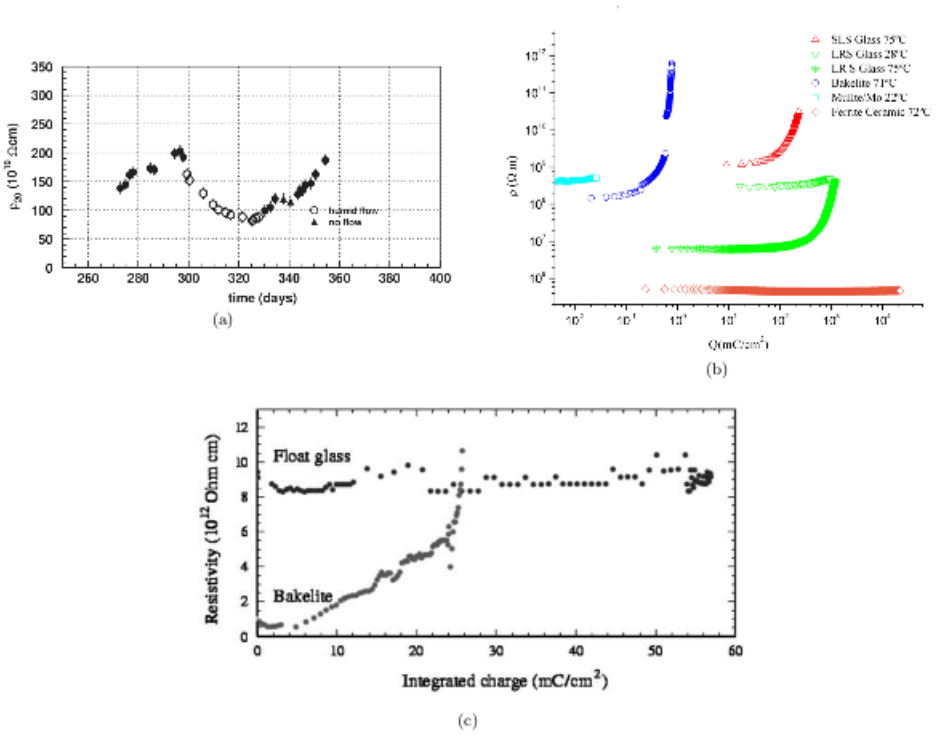

Figure 2.6: (a) Resistivity behaviour change of bakelite when water vapour is added in RPC [43]. (b) Resisitivity comparison for different type of electrode material in function of the integrated charge. The most constant one is the ceramic electrode [44].(c) Comparison between float glass and bakelite. The float glass seems to be a better material to deal with the ageing feature of RPCs [46].

Table 2.1: Comparison between several electrode materials

Electrode material	Bulk resisitivity (Ωcm)	Pros	Cons
Glass	$10^{12} - 10^{14}$	Low-cost Smooth surface No ageing effects	Fragile to HF radicals Limited rate capability
Bakelite	$10^{10} - 10^{11}$	Low-cost Low resistivity Noise reduced	Limited rate capability Lindseed oil treatment needed Humidity needed Ageing effects
Ceramics	$10^{8} - 10^{10}$	High rate capability No ageing effects	Need to be investigated at low temperatures

We connect the high voltage on the painted sides of plates in order to distribute correctely the high voltage accross the whole surface.

Several coatings exist but usually it is a conductive paper or a graphite paint that has a specific resistance defined by :

$$R = \frac{\rho}{t} \times \frac{L}{W} = R_S \times \frac{L}{W}, \tag{2.16}$$

where,
R_S : Sheet resistance = Special case of resistivity for a uniform sheet thickness. Unit in "Ohms per square" ($\Omega/\square$) but dimensionally equal to an ohm.
L and W : dimensions of the sheet
ρ : Bulk resistivity of the sheet
t : Thickness of the sheet.

Typically, resistive layers of $1M\Omega/\square$ are chosen to reduce as much as possible the cluster size.

2.5 Gas mixture

We use gas mixtures in RPCs because each individual gas carries a specific function and a large impact on the performance of the detector [35].

First we want a ionization target. It is well understood that we need fast electron multiplication, i.e. a gas with a large first Townsend coefficient and a low electron binding coefficient (e.g. freon [49] or argon). This is the reason why we often want the detectors to be tight. Otherwise, some air could enter though air has a large electron attachment coefficient. Secondly, excitation of gas molecules could appear when an ion recombines with an electron leading to the lowering of the spatial resolution by emitting visible or UV photons that could create new ionizations. A category of "quench" gasses exist to absorb these secondary photons (e.g. isobuthane [50]). Finally as the avalanche mode is preferred to the streamer mode in order to deal with high rates, one should choose the appropriate gas mixture. For example, to operate the detector in avalanche regime, we want to avoid sparks and for this purpose, "quench" gassses are used (e.g. SF6) [51]. Unfortunately, SF6 has a bad impact on the global warming. Since then some studies are conducted through the world to find an "eco-friendly" gas mixture without compromising the performance of our detectors [52] [53]. This is a real challenge because the recent restrictions deriving from the application of the Kyoto protocol[1] will probably forbid very soon the gas mixtures used in RPCs systems of the LHC experiments.

The table 2.2 lists the two most used gas mixtures in RPCs.

[1] https://unfccc.int/process/the-kyoto-protocol

Table 2.2: Gas mixtures used in common RPCs

Mode	Mixing gas	Example
Streamer	Ar (60.6%) + $C_2H_2F_4$ (34.7%) + iC_4H_{10} (4.7%)	BaBar RPC
Avalanche	$C_2H_2F_4$ (95.2%) + iC_4H_{10} (4.5%) + SF_6 (0.3%)	CMS RPC

2.6 Readout electronics

Reading a singal from a RPC requires some specific features. The readout will mostly depend on the application that we want to make by means of a RPC.

For example, in the CMS experiment [2], a large number of RPCs are used in avalanche mode as a muon tracking system. They operate in this regime because they are in a high radiation environment and the recharge time has to be as low as possible which could not be achieved in streamer mode. However, it means that the resulting electric field is not very high and the gas amplification of the primary electrons is smaller. As a result, the signals are weak and need to be electronically preamplified if we want to read something. For that purpose, front-end electronics has been designed to amplify the signal and then convert it into a logical signal.

The amplification part is very important because it tells us about our detector efficiency : the more amplified the signal, the smaller the incoming signals. This means that the smaller the deposited charge, the higher the rate capability.

2.7 Performance and efficiency

2.7.1 Detection efficiency

The detection efficiency in RPCs is mainly set by the gas gain. This means that the gap width g and the gas mixture play a major role [48] [35].

On one hand, by modifiying the gap width, we change the charge distribution because it depends on the electrical field inside the gap and hence the gas multiplication is affected. In fig. 2.7, we see that we have more events with small induced charge in narrow gap than in wide gap but the signal need to be much amplified in that case. In this case, η stands for the effective Townsend coefficient, the Towsend coefficient α minus the attachment coefficient β. In addition, it would require low thresholds and low noise, thus wide gaps are more efficient in that way. Obviously, electrons created too close to the anode will induce a very small signal that may be not detected with our threshold set by the readout system even if it is preamplified. Henceforth, electrons initiating the avalanche at the opposite of anode will create the largest signals.

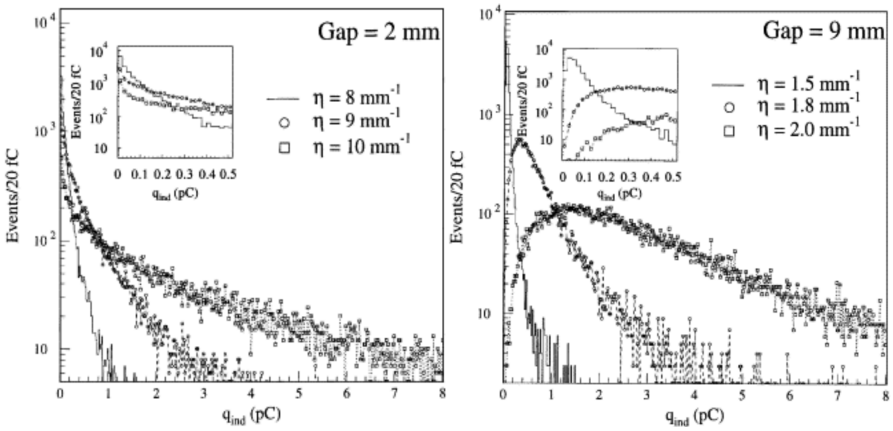

Figure 2.7: Simulated spectra of induced charge, for two single-gap width configuration and different values for the effective Townsend coefficient η [54]

However, one has to take into account the time resolution. Indeed, if the gap used is too wide, then the electrons produced by ionization will take more time to cross the entire gas gap to reach the electrode. In addition, if we use narrow gaps, the gain factor can grow very rapidly even if we have only few micrometers variations [55].

On the other hand, as we said earlier, the composition of the gas mixture has a major impact on the efficiency. We choose an ionization target with the largest Townsend coefficient α, i.e. multiplication factor, but also some quench gasses to suppress the streamers and UV photons.

Another factor that we must take into account when we talk about efficiency is the resistivity of the electrode (section 2.3). Aging effects caused by high rate of radiations will lower the efficiency because the resistivity is increased.

Finally, the temperature and pressure of the medium also affect the efficiency in the sense that if they are modified, then the density of the gas is changed which requires an adaptation of the high voltage applied. For example if the temperature is decreased, then the gas density increases and the electrons take more time to reach the electrode. We have to increase the high voltage to compensate.

If we take into account these factors, we can calculate the effective high voltage as follows [56]:

$$HV_{eff}(P,T) = HV\frac{P_0}{P}\frac{T}{T_0}; \tag{2.17}$$

$$HV_{gap} = HV_{eff} - 2RI; \tag{2.18}$$

where,
P_0, T_0 : Reference parameters
$R = \frac{\rho d}{S}$: Electrode resistance with S, the electrode surface and d, its thickness
I : Total current flowing

Eq. (2.17) gives the high voltage across the gap [57] and rescale the first one in case of voltage dropping induced by the small current flowing on the electrodes.

To describe the detection efficiency i.e, the ratio of detected particles and incident particles, a sigmoidal function response (see fig. 2.8) is often used and defined as [56]:

$$\epsilon = \frac{\epsilon_{max}}{1 + e^{-\lambda(HV_{eff} - HV_{50\%})}}, \tag{2.19}$$

where,
ϵ_{max} : efficiency for $HV \to \infty$
$HV_{50\%}$: high voltage value for which $\epsilon = \frac{\epsilon_{max}}{2}$
λ : coefficient proportional to the sigmoid slope at the inflection point.

If we interpret this equation, we understand that for small high voltage values, the efficiency is null. From a certain threshold value, the efficiency grows rapidly to reach a plateau ϵ_{max}. Normally if we still increase the high voltage when we are in the plateau, we should reach an efficiency dropping and the eq. (2.18) is no longer valid at that point.

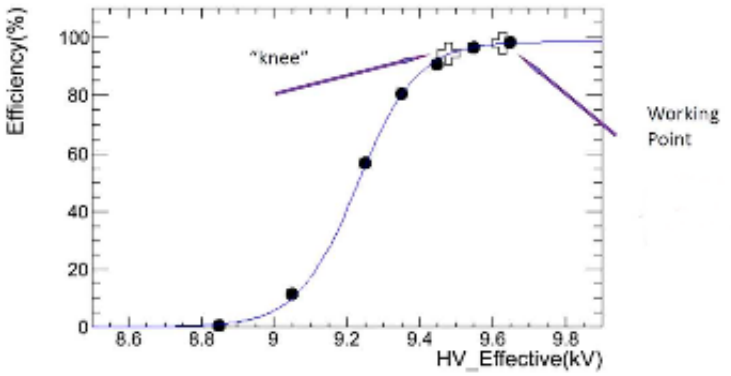

Figure 2.8: Efficiency versus effective high voltage according to eq. (2.18) [56]

The operating high voltage is often chosen as the knee of this sigmoid, i.e, the point where ϵ reaches 95% of ϵ_{max}, in order to avoid the streamers appearing at a certain threshold of high voltage that lower the efficiency.

Finally, the width of the operating plateau gives us an information of the variations tolerated for the gap width.

2.7.2 Time and spatial resolution

Timing performance of RPC's is well-known to be excellent.

If we take into account the extended Ramo theorem (section 2.2.2) and the gas multiplication, the time resolution can be defined as follows [58] :

$$\sigma_t = \frac{1.28}{\alpha - \beta} \frac{1}{v_D}, \tag{2.20}$$

where,

α : First Townsend coefficient
η : Attachement coefficient
v_D : Drift velocity of electrons.

Typically, with a 2-mm gap and standard gas mixture of RPCs $\alpha \simeq 15$, $\eta \simeq 4$ and $v_D = 100 \mu m/ns$, we could achieve a time resolution of $\sigma_t \simeq 1ns$!

Regarding the spatial resolution, it is usually quite good in RPCs ($O(1cm)$) but it depends on several parameters : mainly the strip width and the mean cluster size, i.e the number of strips hit simultaneously, that is directly related to resistivity of the plates (see section 2.3 and 2.4). Indeed the resistive coating will spread the signal which will decrease the spatial resolution. However if the resistivity of the layer is too high, we would face problems with the recharge time and voltage drop. It is then very important to find the good compromise to balance the effects.

In the context of this thesis, excellent time resolution is not yet an important requirement. However, in the next steps of the project, we may want to use timing for background rejection. Hence, the timing would matter. Also space resolution is also important because we would like to make thinner strips in the future. The subject will be more elaborated in chapter 5.

To conclude, this chapter presented the working principle of resistive plate chambers since it was the technology chosen. Its physical characteristics (gas, resistive coating, electrode material, ...) and main properties (performance, signal formation, ...) were described in details in order to understand its operation.

Now we are ready to attack the description of the construction of the muon telescope based on resistive plate chambers that we built at UCL.

CHAPTER 3

Mini g-RPCs prototype

This chapter is dedicated to the setting-up of the mini glass-Resistive Plate Chambers prototype at Université catholique de Louvain. We start from the construction of the detector and its operation to collect data. Then we are dealing with the data analysis that we could perform.

3.1 Construction

3.1.1 Physical layer

The physical layer is about the entire mechanical work that has been done in order to build the detector. We start from the outer shell to the inner shell and then put the whole thing together.

1. **RPC**

- **Detector casing**

  An aluminum box (fig. 3.1) with dimensions 38×29 cm² has been built in order to contain the detector. One should notice the holes that are used to connect the high voltage, the gas inlets and the readout strips. Drawings realized by Nicolas Szilazi are available on a Github repository[1].

  Four metallic boxes have been constructed all in all. The detector casing built in this way is supposed to be **gas tight**. Tightness tests were performed with a vacuum pump. It measured the leakage percentage of the detector and then with helium we were able to find out potential leaks. Each time we have performed this test, we could see which piece had to be changed or modified. For example, we had to apply soldering points on the PCB connector because there were holes that let the helium pass through. Also we decided to apply vacuum grease on the seal each time we opened the detector. The vacuum tests permitted us to achieve 10^{-9} mbar·l/s in leak rate (against 10^{-4} mbar·l/s with the first tests) which is very good and allow to define our detectors as gas-tight.

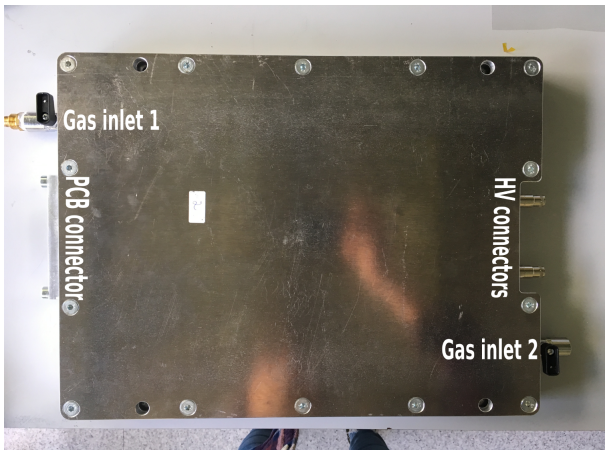

Figure 3.1: Aluminum box

- **Glass plates and resistive coating**

  We decided to choose glass plates for the electrode material for several reasons :
  1) Studies have already demonstrated that glass plates are appropriate in RPCs [44]
  2) They are cheap
  3) They do not require a lindseed oil treatment like bakelite plates
  4) They are not as fragile as ceramics.
  Since we are not dealing with high rate events, we did not worry about ageing effects.

[1] `https://github.com/sowuy/User-Guide.git`

Ordered in France at *Verrerie Villeurbannaise*[2], the glass plates were cut in a square shape of 20x20 cm^2 and 1.1 mm thick.

Obviously, glass plates are initially perfect insulators and could not equalize the high voltage applied over them. As a result, it would lead to inhomogenous electric fields if we use them as high voltage electrodes (see section 2.3).

To remedy to that, we applied some paint to lower the resistivity of the glass plates (fig. 3.2). In this way, the applied high voltage is uniformly spread and a "capacitance" is given to the electrodes such that the gap can easily recharge after an ionizing event.

The mixture is made up of paint and methanol (which evaporates when it is painted) 3cc each. We used a magnetic stirrer to mix both. The paint in itself consists of *CPM10C Colloidal Dispersion* which comprises a colloidal dispersion of antimony-doped tin oxide in water - proportions of 20 of powder for 80 of water. After thoroughly cleaning the glass plates, we use a roller to apply a uniform coating on them. In order to keep the edge spacers out of the active region (related to the strips size), we made a masking tape with kapton tape.

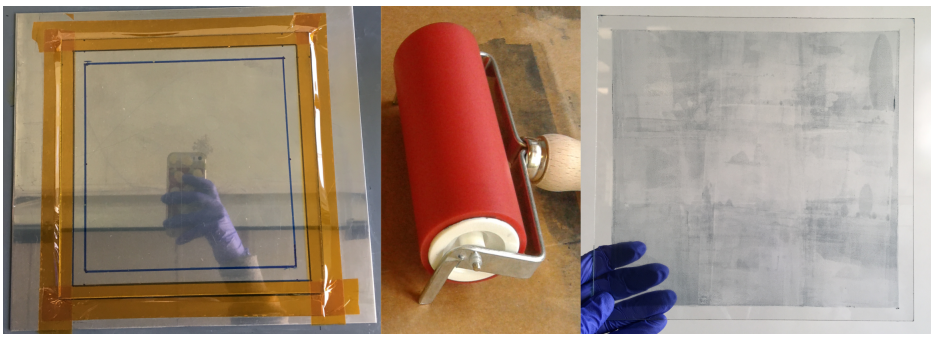

Figure 3.2: Method to apply the resistive coating on glass plates

- **Gas gap construction**

  Once the resistive coating has been applied, we can deal with the gas gap construction. To ensure its uniform width, nine round edge spacers made in PEEK (Polyether ether ketone) are used between the glass sheets as shown in fig. 3.3.

  We have flat round spacers with diameter of 2cm and 1.1mm thick and non-flat ones. The latter are 1.1mm thick on the outer corona and 3.1 mm thick on the inner corona with 1.1cm of diameter. They are used to construct the gap between the glass plates (which will be 1.1mm wide obviously). The fact they are not flat

[2] `http://www.verrerie-villeurbannaise.com/fr`

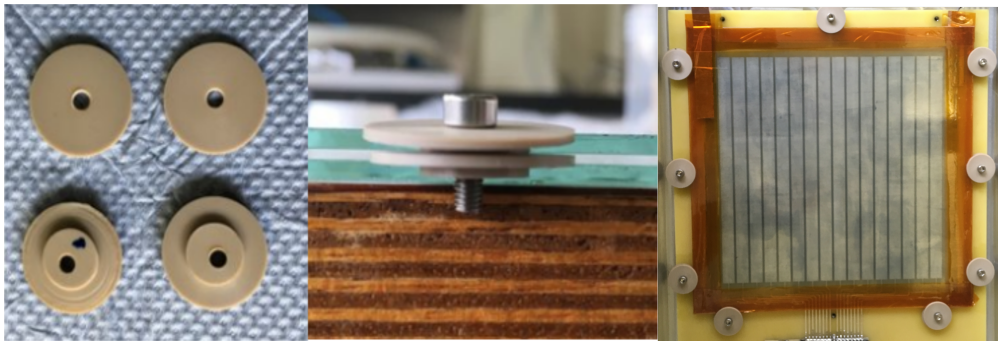

Figure 3.3: Round edge spacers

helps to wedge the glass plates in the appropriate way. The flat spacers are then placed on the top of the second plate and we can screw them together inside the box (holes in the detector casing were provided for that).

The drawings are again available on github[1].

- **Printed circuit board and readout strips**

  The design of the printed circuit boards (PCB) include 16 strips 16 cm long with a pitch of 1cm (fig. 3.4). A jumper (not visible on the figure) is soldered on the metallic band near the readout. It is placed there to make a connection between the masses of the high voltage and the readout strips. Its primary function is to avoid mass loops. One could notice the holes in order to fix the PCB inside the detector casing with small screws. The readout wires are connected to an adapter board for connection with a front-end board equal to those used in the CMS experiment [2].

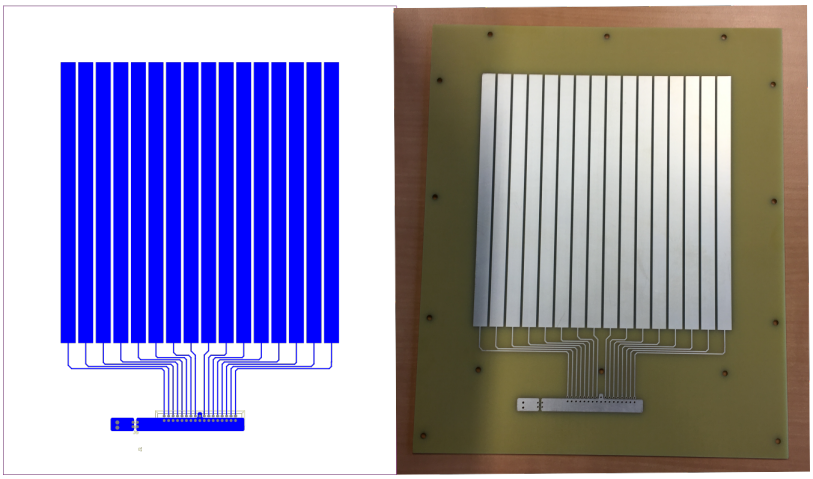

Figure 3.4: Printed circuit board made by Daniel Michotte. Left : Drawing. Right : Physical PCB

A PCB piece is interleft between the hole in the detector casing and a metallic piece provided for the purpose (see fig. 3.5).

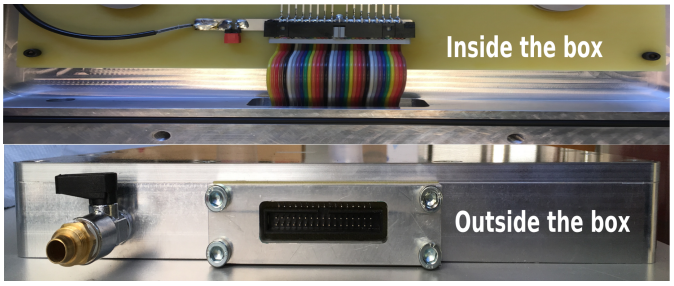

Figure 3.5: PCB piece

- **High voltage connection**

  In order to make the high voltage connection, we soldered the wire to the HV connector and to the resistive coating in order to spread the high voltage accross the plates (fig. 3.6). We use the same procedure for the electrode grounded. To insulate the inactive part of the glass plates, we use dielectric tape (Kapton tape).

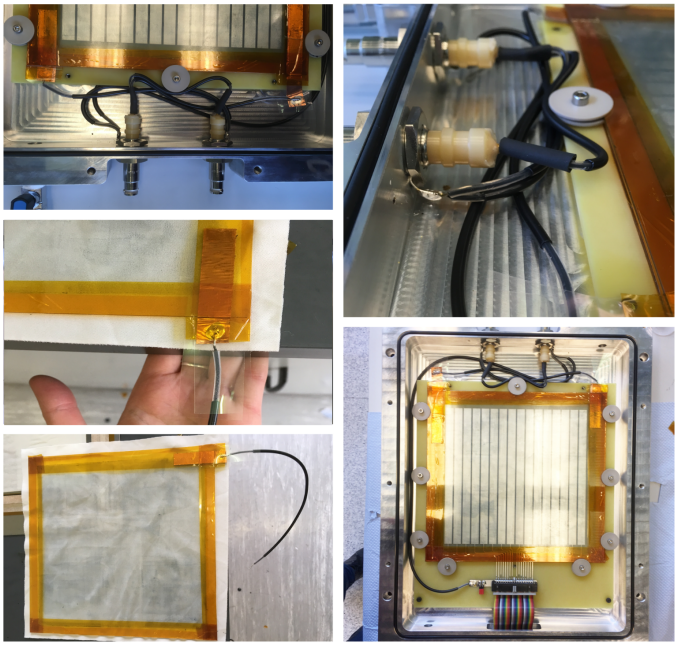

Figure 3.6: HV Connection

2. **Electronics**

- **Readout electronics**

  Global description

  For convenience, we took CMS RPC front-end electronics [59] borrowed from University of Ghent and initially used for the RPCs at CMS. It consists of a front-end amplifier-discriminator-monostable integrated circuit (see fig. 3.7).

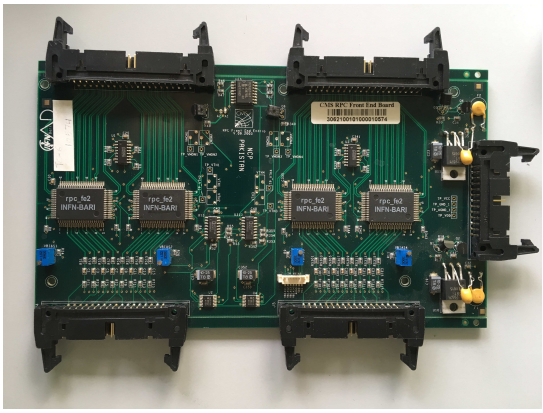

Figure 3.7: CMS RPC Front End Board

This device is installed on an electronic board [60] that first amplifies and discriminates the induced signals from the RPC readout strips and then sends digitized signals to the Trigger Electronics (FPGA) via twisted pair cables.

Each front-end board (FEB) has 4 chips, containing 8 channels which gives us a total of 32 channels. Therefore one FEB is used for 2 chambers.

Each channel consists in an amplifier with a charge sensitivity of 2mV/fC, a discriminator, a monostable and a LVDS driver. A single channel block diagram is shown in fig. 3.8).

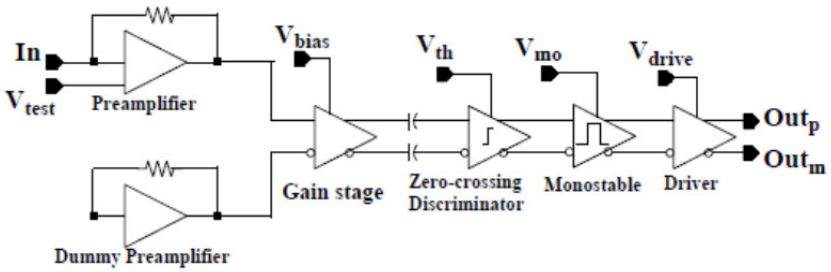

Figure 3.8: Diagram of one channel of the CMS RPC FEE [59]

Characteristics :

Threshold

Four variables control the threshold values. We can program them via a DAC or potentiometers. For fear of burning the chip, we didn't use them together and the potentiometers were then unsoldered.

Pulse width regulator

The monostable controls the output signal duration. In addition, if we get two current pulses related to only one physical event (with time separation of 0-100 ns), the monostable will not consider the second pulse. The default pulse width regulation is 3.5 V (corresponding to 100 ns pulse width).

ADC [61]/DAC [62]

For each chip (4 on 1 board), there are 2 DACs and 2 ADCs. The DACs allow the programming of the thresholds and the monostables. The values needed for thresholds and monostable are entered manually in the I^2C interface and via the I^2C serial Bus, it transfers the analog information and the DAC sends the digitized information to the chip. Whereas the ADCs are just there in order to control the output of the DACs.

Pinning schemas of FEE, ADCs, DACs are available on github[1].

- **High Voltage**

  Regarding the high voltage, we had to face a last-minute change.
  The HV module bought has a negative polarity however, we realized two things :

  (a) Muon signals seen on the oscilloscope are negative

  (b) Signals expected and read by the readout system are positive

  Therefore we couldn't read the muon events with a negative HV module.

  A positive HV[3] (0-20kV, 1.5 mA) was found and we adapted it to our system without changing anything in the control program.

  The description of the negative HV remains relevant since in the future we should replace our old and noisy readout system with a new chip (like HARDROCK 3B[4]) that expects a negative signal). This will be elaborated in chapter 5.

[3] http://www.fug-elektronik.de/en/products/cassettes/hce.html
[4] https://www.weeroc.com/en/products/hardroc-3b

- **DPS module [63]**
  This device is a supply module system capable of high voltage power. It is controlled by HV power supplies. Our DPS module is mini model one (500 V $\rightarrow$ 10 kV). Output voltage is controlled via analog interface.
- **HV module controlling**
  - PCF8574 Remote 8-bit I/O Expander for I^2C Bus [64]
  This device is the power switch of HV .
  - AD5593R - ADC/DAC [65]
  The AD5593R is an 8-channel, independently configurable analog and digital I/O port. The ADCs are there in order to give a control of IMON and VMON whereas DACs are there to provide values for ISET and VSET written by the user.

3. **Assembly**

The final assembly of four detectors is shown on fig. 3.9. The PCB is firstly fixed inside the metallic box. Then the first glass plate is put on top of the PCB. Next, the gas gap is constructed and the voltage connections are made. In this way, there is no contact between the glass plate (grounded) and the strips (due to the kapton tape). As a proof, we measured the resistance between the strips in a chamber and it was always infinite as expected. We used vertical bars in order to create a distance between the four detectors to play with the angular resolution and acceptance.

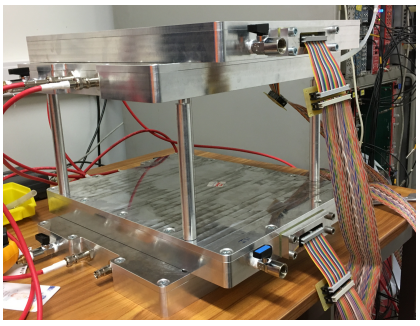

(a) With spacers

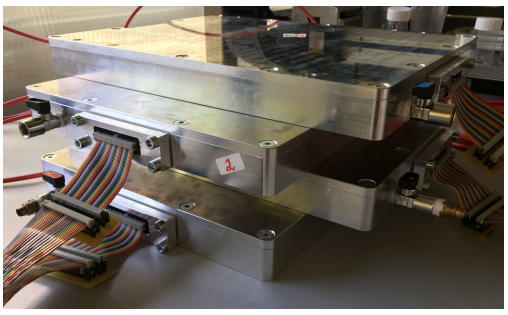

(b) Without spacers

Figure 3.9: Mechanical assembly with and without bar spacers

In the rack (fig. 3.10), there are all the electronic components defined in the previous section, i.e. CMS RPC Front End Board (2) with each 4 chips on it, the HV module, DACs, ADCs but also the FPGA we used in order to program the whole thing and the CPU that is used to perform computer tasks.

The configuration of 2 detectors operating is shown in fig. 3.11.

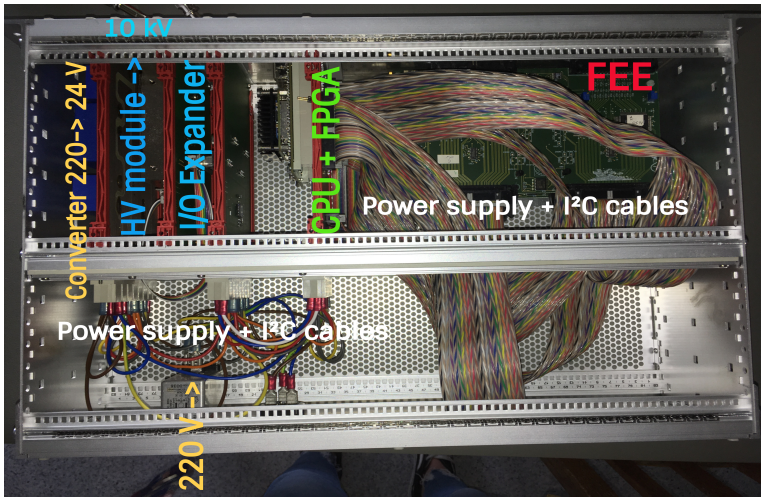

Figure 3.10: HV and readout system placed in a rack

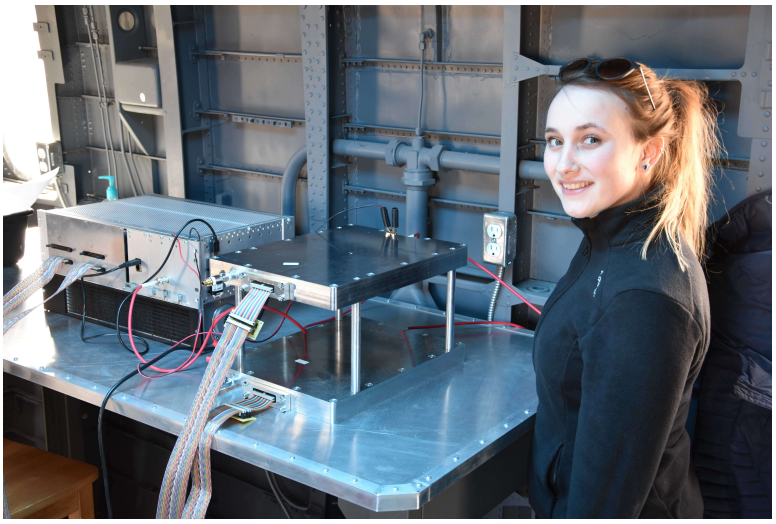

Figure 3.11: Me next to two detectors configuration used at the Mars Desert Research Station (Utah Desert) for UCL to Mars 2018 mission

3.1.2 Logical layer

1. Acquisition process

   Acquisition of information happen, by picking up the electrical signal induced by the ion pairs avalanche inside the gap as explained in section 1.1. Once a pulse is detected, a time window of 80 ns opens and all pulses that happen during this period of time are added (OR-operation between all channels together)

   Given that the electric field is quite low, the signals acquired in the avalanche mode are relatively weak and to remedy to it, preamplifiers need to be used. That is where the front-end electronics occur : they constitute the electronics that amplifies the incoming signal of the RPCs and convert it into a logical signal.

2. Thresholds

   The thresholds are crucial in our muon detection system. Indeed, an event (depending on the number of coincidences entered) is when a muon fires a strip and the signal exceeds the threshold written in the configuration.

   The values written in the interface are in arbitrary units. In order to find the pure and irreducible electronic noise, one can operate the detector with 0 V and look for the threshold value from which the detector won't be affected by events induced by the noise.

On fig. 3.12, one can find the high level schema of the electronic part of the detector. Three main blocks are displayed : HV control, CMS FEE and "Brain" of detector. The brain contains the CPU and the FPGA and controls everything. It is programmed depending on the needs. Here, we have two needs : the control of the readout and the control of the high voltage. RPC readout strips send their signal to the chips that decide if the signal is kept or not depending on the threshold and monostable entered. The high voltage is switch on with the I/O expander. Values (ISET, VSET) are entered via the I^2C interface and are controlled by the ADCs. It provides a high voltage output between 0 and 10kV connected to the high voltage connectors of the chambers. Finally, a wifi antenna connected with a USB to the CPU allows to collect data easily.

3.2 Data collection

3.2.1 At the Mars Desert Research Station

Once the construction of the first detectors was finished, the data acquisition part could start.

The first data campaign has been led in march 2018 in the context of "UCL to Mars 2018"[5], a life on Mars simulation at the Mars Desert Research Station (MDRS) in the Utah desert (USA) to which I've been taking part as a crew physicist during two weeks. Fig. 3.17a shows a picture of me installing the detectors in the desert. I have a spacesuit to simulate the conditions that an astronaut is subject to.

At that time only two out of the four detectors were operational but we decided to ship them to the USA anyway to test them. The chambers were assumed to be filled with a mixture of argon (95.2%), SF_6(0.3%) and isobuthane (4.5%) with the gas system present in the cyclotron building before the trip with a pressure a little above atmospheric pressure. The PCB of one of the two detectors had a jumper. Two crucial issues affected the collection of these data: the fractions of SF_6 and isobuthane were not as expected, resulting in numerous sparks and the impossibility of a satisfactory optimisation of high voltage and thresholds, and there was

[5] http://www.ucltomars.org/

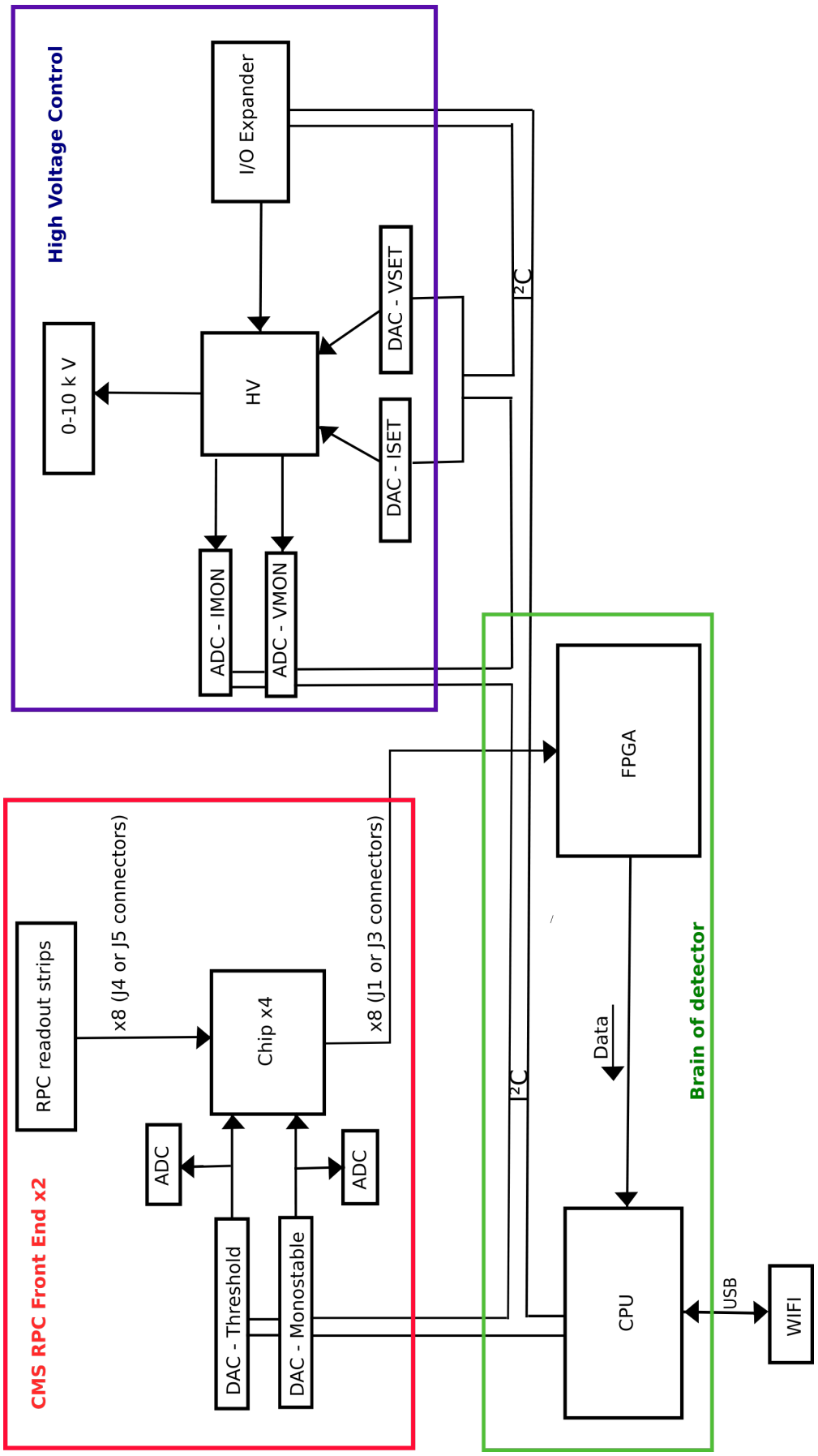

Figure 3.12: High level schema ©Sophie Wuyckens

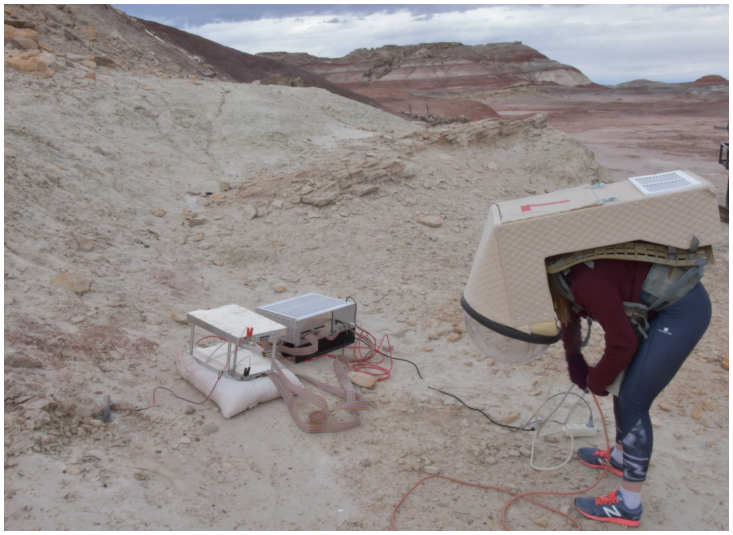

Figure 3.13: Two detectors collecting data in real conditions in the Utah desert.

a very large ambient noise, picked up from a power generator. The sparks had the effect to trigger all the strips as if the detector was in streamer mode. To solve the noise issue, I tried to move away the detector at different locations to solve the problem. I also tried to use a real ground connection by digging a hole in the ground and placing a metallic rod in it with salted water to reduce the noise. But these solutions weren't enough to obtain clear real data.

The tests that were performed over there were the following :

1) Study the event rate for each detector separately (no. 1 or no.2).
2) Study the event rate for both detectors in coincidence (no. 1 and no. 2)
3) Perform scanning in high voltage and thresholds for configuration 1) or 2).

The third test can be explained as follows: When the setup is ready to start data acquisition, it is interesting (when it is the first time the detector is used) to find the operating plateau of the detector (see Section 2.7.1). It means that from a given value of high voltage, the detector will behave properly and will be good at detecting muons. The same thing applied for thresholds, one has to find the optimal thresholds in order to dismiss the background while keeping muon signals.

Although the results obtained at MDRS have no scientific value, these experiments allowed us to verify several specific features of the detectors design :

- **Gas-tightness** : Before filling the detector casings with the operating gas, tightness tests were performed by measuring the leakage rate after creating vacuum and looking for leaking points with helium. It revealed several defects in two detectors at the level of the PCB connector and HV connectors and time was missing to fix them. This is why only two out of the four detectors were shipped. Following my return, I measured the pressure in both detectors taken for the mission, and they didn't lose any pressure from the day of sending.

- **Portability and compactness**: The detectors have been sent from UCL in Belgium to the middle of Utah Desert in USA. A box made in wood (60x40x69cm) shipped both detectors, the rack with electronics (high voltage and readout system), a transformer and useful tooling for a total of 37.5 kg. Over there, I operated the detectors inside the station but also outside without any help of my crew members thanks to the ease of the carriage. One detector weighs 6.5 kg.
- **Robustness** : As said previously, the detectors survived a round trip between Belgium and USA without any problems. They were working over there and are still working today. They collected data outside the station sometimes with strong wind or high temperatures, demonstrating their efficient operation in adverse environmental conditions.

3.2.2 At University of Ghent

Upon return of the detectors to Belgium, we addressed the issues that affected the quality of data at the MDRS.

We realised that the problem with the gas behaviour could be traced back to an issue with the gas mixing system in our laboratory, which will need a refurbishment.

Therefore, the four detectors being operational were taken to University of Ghent where they were filled with the local gas system. The gas mixing was the same as the one used at UCL except they use Freon as ionization target instead of Argon. The proportions were also the same. Over there, we tested each detectors separately with the coincidence of two scintillators. The setup used is shown on fig. 3.14. The scintillators are placed one over another to maximize acceptance for the coincidence. Three channels (0, 8 and 9) of one chamber were spied. With our negative high voltage module, we actually saw muon events that induced negative signals (blue signal).

These tests showed us some problems that forced the modification of some chambers before data-taking. Indeed, one of the chamber has its PCB piece mounted upside down and as a consequence all the pins were connected between them and thus connected to the ground, giving chaotic signals on the oscilloscope.

We also realised that the problem with environmental noise was due to the usage of jumpers, which were then taken off. In that way, the ground of the electronics was no longer connected to the high voltage ground in the chamber.

After that, we continued the studies in our laboratory at UCL.

3.2.3 At Université catholique de Louvain

Back to UCL, we wanted to perform the same tests with the addition of our readout system .

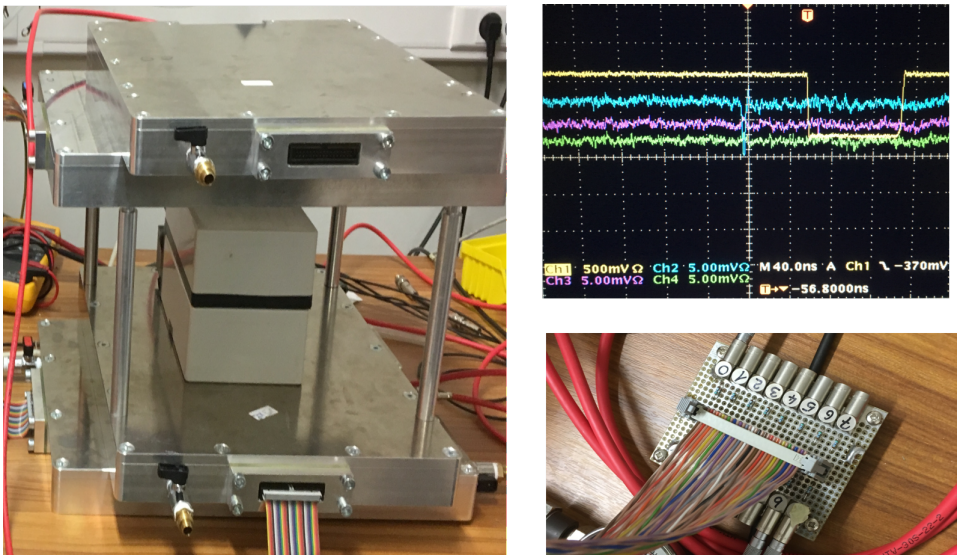

Figure 3.14: Setup used in Ghent. Oscillogram : Yellow : coincidence of scintillators. Blue : muon negative signal. Pink : Crosstalk on neighbour strip. Green : Channel 0 not triggered.

Two small and very clean scintillators in the CMS-upgrade lab were used to do some tests. The setup is shown in fig.3.15.

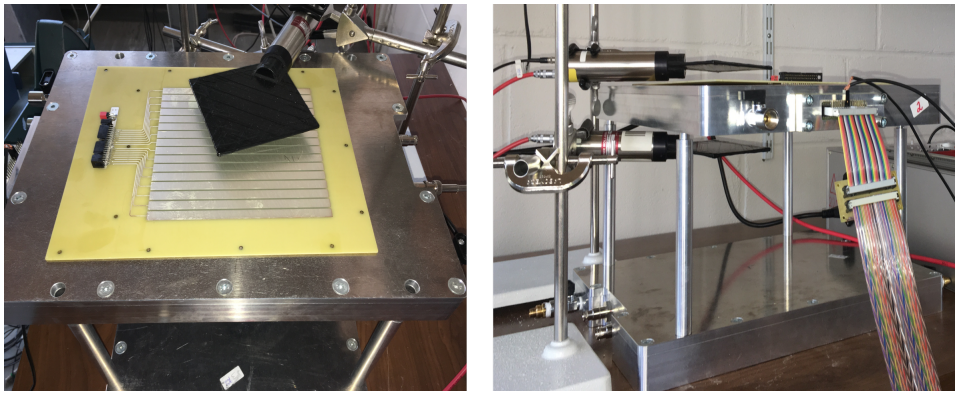

Figure 3.15: Setup used in the CMS upgrade lab at UCL

We rapidly realized that the polarity of our readout system was not the right one. Our readout system reads positive signals and not negative ones. Therefore we think the system was triggering mainly on the crosstalks created by muon events on neighbouring strips and positive noise.

The high voltage module has been changed for a positive one. From that moment, we have seen a lot of clear muon events. Fig. 3.16 shows an oscillogram obtained with the setup. Three neighbouring channels are connected to the oscilloscope and one channel is the digital trigger from the readout system (not shown on the figure). The muon event is the positive blue signal whereas the two other signals are interpreted as crosstalk. The signal lasts $\sim$ 14 ns (time

width) and is around 100mV. The signal is followed by reflections due to wrong impedance matching in the cables. This will be fixed at some point in the future.

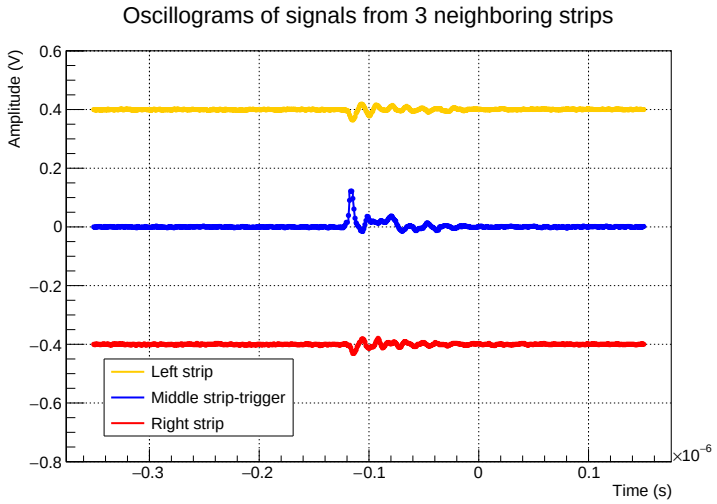

Figure 3.16: Oscillogram obtained of a clear muon event at $\sim$ 6.5kV

The evolution of events according to the major modifications made to the detectors during the semester can be visualized in fig. 3.17. This figure shows in three cases an illustrative event from the data, with the reconstructed trajectory of a muon giving signal in all planes. Fig. 3.17a is a typical event obtained at MDRS. All the strips of both detectors are triggered and we cannot extract any information from it. In addition, the high voltage could not be set very high otherwise sparks appeared. The gas mixture was then changed at UGent and we obtained, fig 3.17b that shows a typical event obtained at UCL when a negative high voltage was used. The fit seems to pass through the holes between the triggered strips. Finally, fig. 3.17c shows a very clear event obtained with positive high voltage.

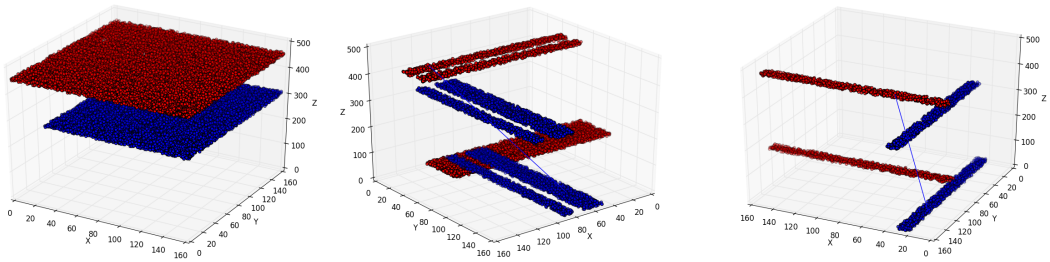

(a) @MDRS - 4.5kV & th 100

(b) @UCL with negative HV - 6.8 kV & th 100

(c) @UCL with positive HV - 6.6 kV & th 105

Figure 3.17: Event display

These data displays are only specific examples to draw your attention at the final purity of events that could have been reached with the modification of the setup but we obtain bad data in each case due to noise.

3.3 Data analysis

For all the following studies, **4** detectors were used each time in coincidence with no spaces between them to increase the acceptance to its maximum and get a high event rate (fig. 3.9 on the right). They were self-triggering.

3.3.1 Operating voltage and threshold

Once we were able to see real muon events, we could re-use the shell scripts developped for scanning in high voltage and threshold.

For each high voltage value and for each threshold value entered, data were collected during 10 minutes. The data plots presented in this section come from a scanning study between $HV_{min} = 5.9$ - $HV_{max} = 8.3$ kV with a step of 12 V and $TH_{min} = 90$ - $TH_{max} = 140$ with a step of 5. This makes 200 points in total and thus ≈ 33 hours of data collection.

Fig. 3.18 shows the scanning plots in two dimensions. We see that if we apply cuts on the number of strips touched per detector or on the total number of strips, a certain high voltage and threshold value stand out in muon rate.

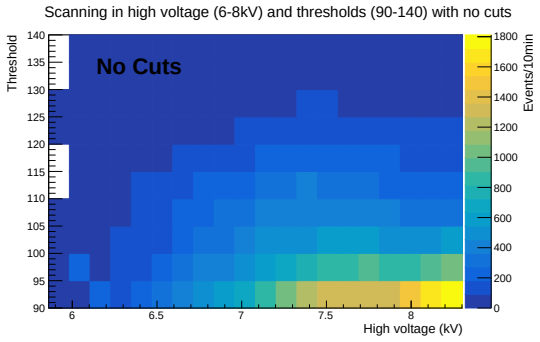

(a) No cuts

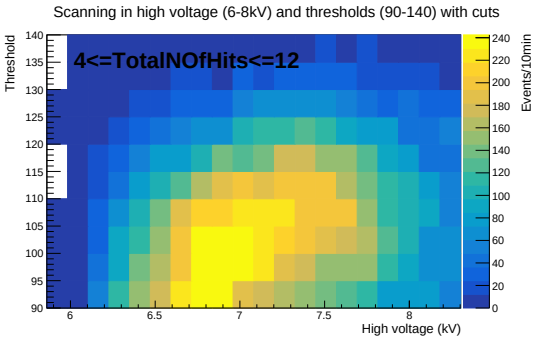

(b) $4 <=$Total Number of hits $<= 12$

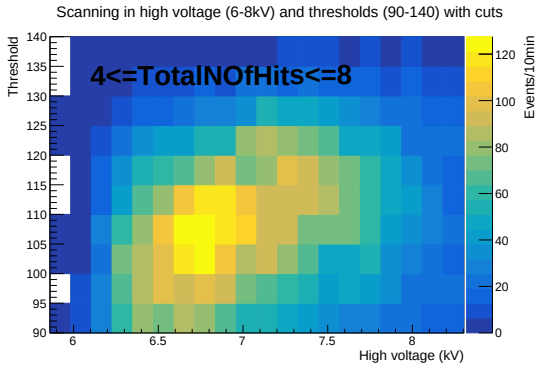

(c) $4 <=$Total Number of hits$<= 12$

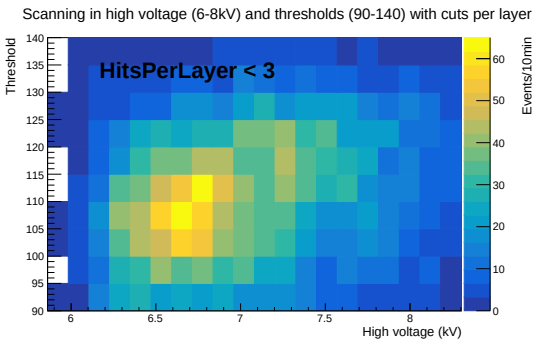

(d) Number of hits per chamber < 3

Figure 3.18: Scans in two dimensions : HV and threshold for different cuts

These cuts are justified as follows. If we look for the number of hits for each events, we see that for the data studied, the maximum of events is obtained when 7 hits are observed in total. This is shown on fig. 3.19

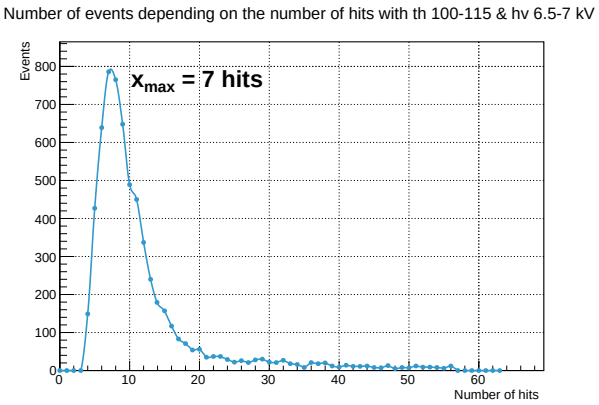

Figure 3.19: Events versus number of strips touched

Finally, if we look at the region where there is the largest number of events in fig. 3.18d, profile plots can be extracted in order to define operating high voltage and thresholds.

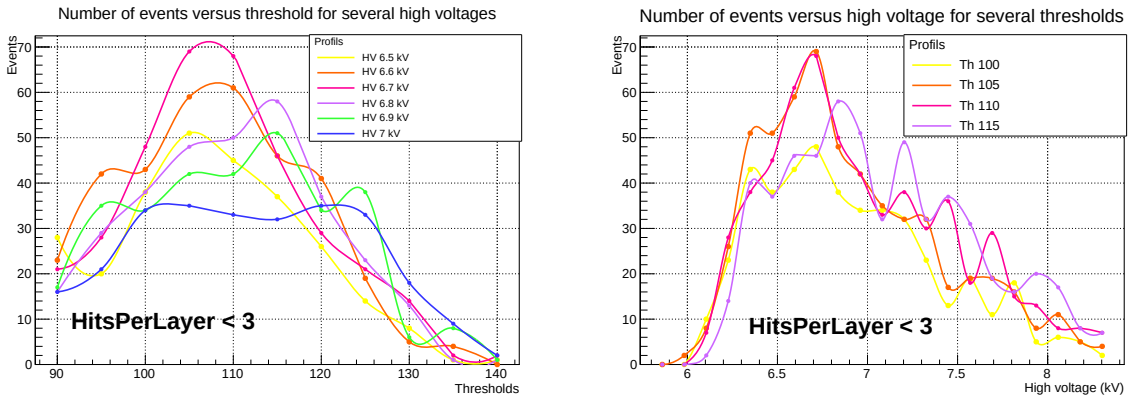

(a) High voltage Profile

(b) Threshold Profile

Figure 3.20: Profile plots in the high muon rate region with cut : Number of hits per chamber strictly less than 3.

As a consequence, fig. 3.20 demonstrates that the most appropriate high voltage and threshold values range between :

$$\boxed{HV = 6.6 - 6.7kV \quad \& \quad TH = 105 - 110}$$

3.3.2 Hits pattern

Once we knew the operating high voltage value and threshold, we could perform long data acquisition to study other features of the chambers.

Among them, hits pattern is interesting to look at. Indeed, it should be uniform, otherwise it could mean that some channels are not working well. For example, this allowed us to exclude from further analysis the first and last strip in each detector since they were found to be very noisy. The comparison between each chamber can also be undertaken with this kind of survey.

The following study comes from a data collection for HV = 6600 V and TH = 105 during 6 days.

Fig. 3.21 shows several plots of hits patterns for different cuts. A general comment that can be done is that endpoints are indeed the most firing for any cuts.

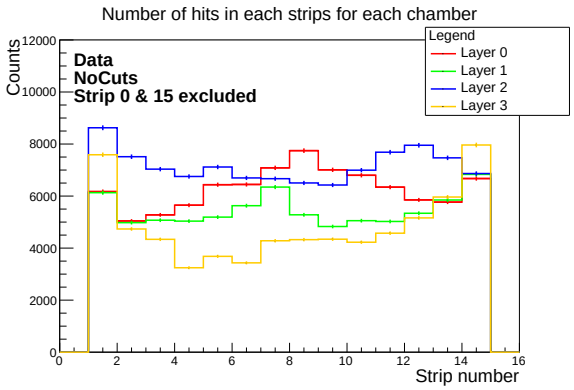

(a) No cuts

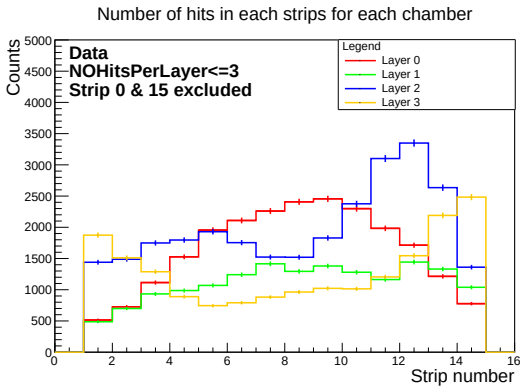

(b) Number of hits per layer less than 3

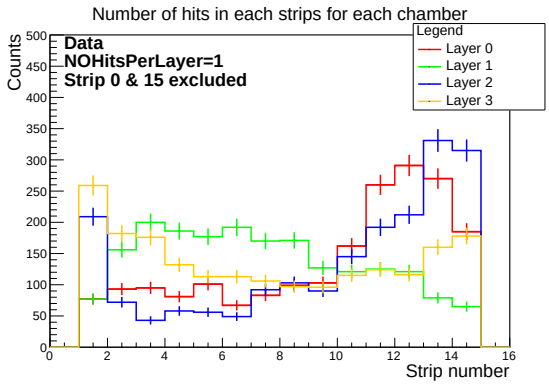

(c) Number of hits per layer equal to 1

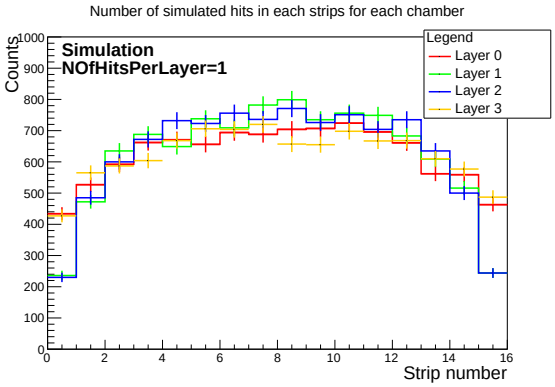

(d) Number of hits per layer

Figure 3.21: (a),(b),(c) : Hits pattern for different cuts @6600V and TH = 105 with strips 0 & 15 excluded. (d) : Simulated data with one hit per chamber

Fig. 3.21d shows a simulation of the expected hits pattern with such a configuration of detectors. It demonstrates by comparison with fig. 3.21c that the expected behaviour is far from

reality for the moment. The hits pattern should follow a parabolic form and this is not observed in data. In addition, with our setup geometry, it makes sense that chambers 1 and 2 (middle ones) are less hit on the edges than chamber 0 and 3. These anomalies should find their origin in the electronics. This assumption is made from the fact that when the high voltage is off, we still continue to observe events. And these events are very often those that have the first or the last strips triggered.

3.3.3 Track reconstruction

With the same set of data, track reconstruction has been performed.

We chose to reconstruct zenith ($0 < \theta < \pi/2$) and azimutal ($0 < \phi < 2\pi$) angles of muon trajectories thanks to the position information of the hit in each chamber.

The script only read "perfect events", i.e. with one hit per chamber.

From that, the touched strip number is converted to a position by using the geometry of the detector. In this way, four coordinates (x_0, y_1, x_2, y_3) obtained from the four chambers directly give the angles of the muon trajectory :

$$\phi = arctan2(\frac{y}{x}) \tag{3.1}$$

$$\theta = arccos(\frac{z}{r}) \tag{3.2}$$

where,
$x = x_2 - x_0$: Distance between touched strips of x-chambers
$y = y_3 - y_1$: Distance between touched strips of y-chambers
$z = 7.4$: Fixed distance between x-chambers or y-chambers
$r = \sqrt{x^2 + y^2 + z^2}$
$arctan2$: This C++ function is basically an arc tangent in the interval $[-\pi, +\pi]$ radians. It takes into account the sign of both arguments in order to determine the quadrant contrary to arctan that has a sign ambiguity.

Eq. (3.1) and (3.2) have been applied on data (6600V, TH=105 and 33hours) and fig. 3.22 show the result.

A few comments about the distributions obtained are written below :

- Zenith angle θ : As explained previously (cfg. section 1.2.4), the distribution expected for the zenith angle should have a form close to $cos^2(\theta)$ with a maximum near $0°$. However, this is not observed in fig. 3.22a. The maximum number of events is around $15°$ with a dip around $0°$. One explanation could be that the geometry of detector has a big effect

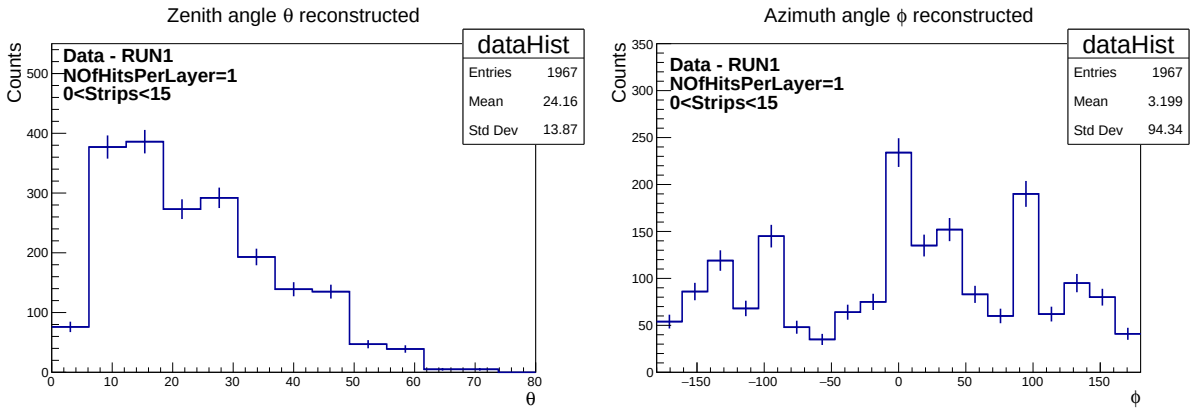

(a) Zenith angle

(b) Azimuth angle

Figure 3.22: Angles reconstructed with cut : Number of hits per chamber equal to 1

on the distribution. This statement will be checked in the next chapter regarding simulation. Another factor that could be taken into account is the amplitude of the signals. It could be larger for "horizontal" muons than for "vertical muons" because the path of the muon would be longer and thus more ion pairs could be created making the signal stronger.

In addition, this angular distribution has some similarities with the one obtained with MURAVES detector [9] as shown in fig. 3.23. This detector is bigger than ours (50x50 cm²) with 6 detection planes and a height of 115cm but it is the same kind of telescope geometry.

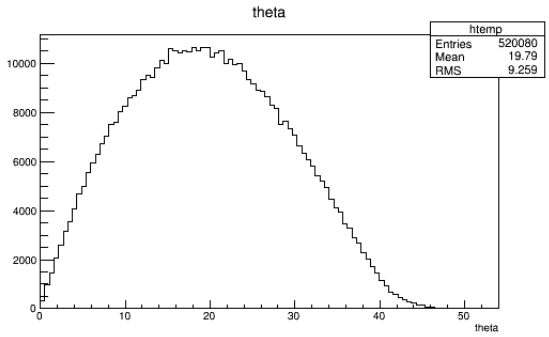

Figure 3.23: Theta distribution obtained with MURAVES detector [9]

- Azimuth angle ϕ : For this distribution, we would expect a flat one because no direction is preferred, there is no physics behind that. But fig. 3.22b shows that trajectory with $\phi = 0°$ is favored. No explanation has been found so far.

In order to check whether these effects originate from the geometry or something else, two tests were undertaken.

One was to turn all the detectors configuration of $90°$, repeat the same analysis with exact same parameters and then compare. Plots of this set of data can be found in Appendix 3.

With this configuration, the behaviour is still the same. As a result, we can say that the particular form of the distribution does not come from an external source in the building. The geometry and the granularity of the detectors still remain the most probable explanations.

Another test is to simulate the geometry of the setup, generate muons and reconstruct their tracks. Chapter 4 will be dealing with this second check.

In this chapter, the development of the mini-gRPCs prototype at UCL was described in details at its physical and logical level. We presented the data campaigns that were conducted during the semester and some of the analyses that could have been performed on it. One important result was the find of the operating voltage and threshold to operate the detectors properly. We could also observe the hits pattern on strips to see if they were all working fine and it was not the case since edge strips have to be ignored due to noise. Finally, we could start to reconstruct the muon tracks and we get a particular zenith angle distribution that could be explained by the geometry of the telescope.

For a more detailed description of the electronics part of the prototype, one can have access to a User Guide written in that respect [66].

In parallel of the development of the mini-gRPCs prototype, some simulations tests were performed and this is the topic of the next chapter.

CHAPTER 4

Simulation

This chapter describes the software part of the project that has been made. It includes simulations of geometrical effects and of the signal induced in such a chamber.

All the scripts written and used in this chapter can be found on github[1].

4.1 Monte Carlo Simulation

In this section, the simulation in itself is explained.

The code of Alexis Fagot (UGent)[2] has been used and modified according to our needs. It is written in C++ and aims at studying the effect of the orientation of a trigger system on the particle distribution on the surface of a vertical or horizontal detector plane.

The modifications made mainly affect the code of the detectors geometry and output files wanted.

This simulation generates a muon (θ, ϕ) in a cosmic plan according to the $cos^2\theta$ distribution and a uniformly random value for ϕ and looks at the intersection with the four chambers. If

[1] `https://github.com/sowuy/Simulation`
[2] `https://github.com/afagot/Cosmic-Distribution`

the muon crosses the four plans of detector and if each intersection is in the detection surface, then we keep the event.

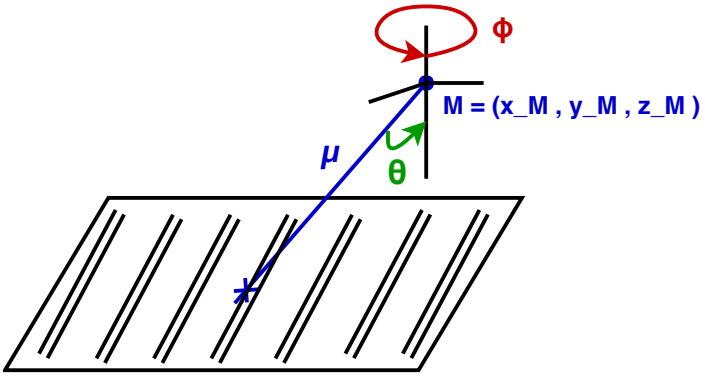

Figure 4.1: Muon μ created at $M(x_M, y_M, z_M)$

To calculate the intersection between the muon direction and the 4 detection planes (fig. 4.1), the following calculations have been made :

Let's $\vec{v} \begin{pmatrix} sin\theta cos\phi \\ sin\theta sin\phi \\ cos\theta \end{pmatrix}$ be the direction vector of the muon μ and $M(x_M, y_M, z_M)$ the position of the muon generated as illustrated in fig. 4.1.

Its equation is given by

$$\mu = \begin{cases} x = sin\theta cos\phi \cdot t + x_M \\ y = sin\theta sin\phi \cdot t + y_M \\ z = cos\theta \cdot t + z_M \end{cases} \tag{4.1}$$

where t is the parameter of the muon trajectory.

The equations of each plane are the following :

Uppermost x-plan n°0 : $z = 2d + w$
y-plan n°1 : $z = w + d$
x-plan n°2: $z = d$
Lowest y-plan n°3 : $z = 0$

where d is the distance between planes n°0 and n°1 or n°2 and n°3 and w is the distance between planes n°1 and n°2.

Thus for example, if want to know the hit position in plane n°3 ($\mu \cap P_3$), we simply have to find the parameter t by solving the equations system made by equation of P_3 and μ and replace t by its value in μ eq. (4.1).

In this particular case, we simply have $\boxed{t = \frac{-z_M}{cos\theta}}$ and thus the hit position is given by :

$$\begin{cases} x = -z_M \frac{sin\theta}{cos\theta} cos\phi + x_M \\ y = -z_M \frac{sin\theta}{cos\theta} sin\phi + y_M \\ z = 0 \end{cases}$$

The same procedure was used to calculate the instersection with the three other planes.

In addition, since the strips are 0.9 cm wide, if for example, the muon touches a strip at 5.42 cm, we convert it to a strip number in the following way : $\frac{5.42}{0.9} = floor[6.02] = 6 \Rightarrow$ Strip 6 touched.

The output files generated by this simulation include histograms of muon triggered position and direction (ROOT files). The parameters entered are the distance w between the plans and the height of cosmic plan H where the muons are generated. Examples of output files are shown in fig. 4.2. It demonstrates that spacers decrease a lot the acceptance of the setup. This effect is quantified in section 4.3.

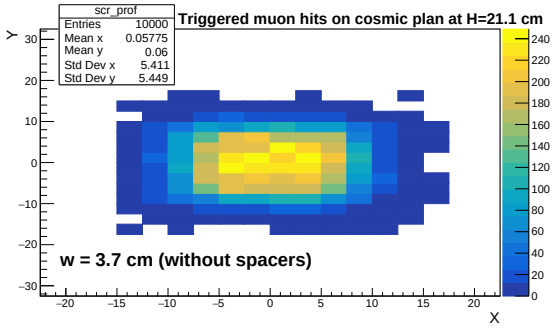

(a) Cosmic plan + no spacers

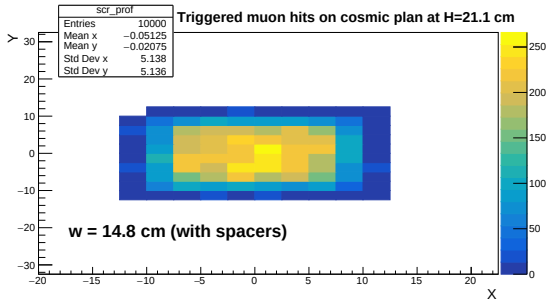

(b) Cosmic plan + spacers

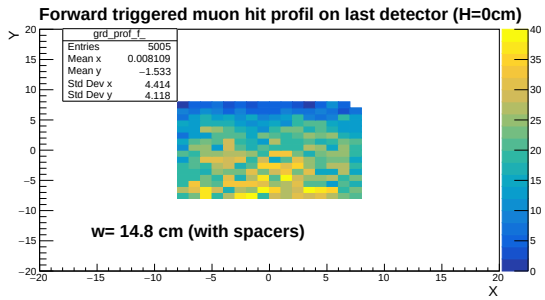

(c) Forward muons ($\phi < \pi$)

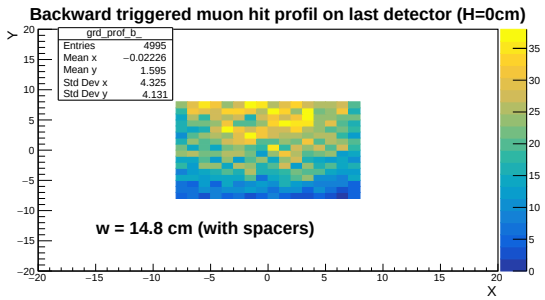

(d) Backward muons ($\phi > \pi$)

Figure 4.2: Simulated hits pattern on cosmic plan and on last detector with and without spacers

It produces also CSV files with all the needed information. The number of the strips touched by the muon in each detector was used in this case. From these files, I created another script (*amplitudecalculator.cpp*) able to calculate the angles from four pieces of information in decimal

format. It was different from the one applied on real data, because the reading is not in binary code this time. A comparison between real data and simulation could be done and is shown in fig. 4.3. Fig. 4.3a shows that our data does not agree well with simulation. There are large fluctuations between both histograms whereas fig. 4.3b seems to agree better, still with this strange peak at zero.

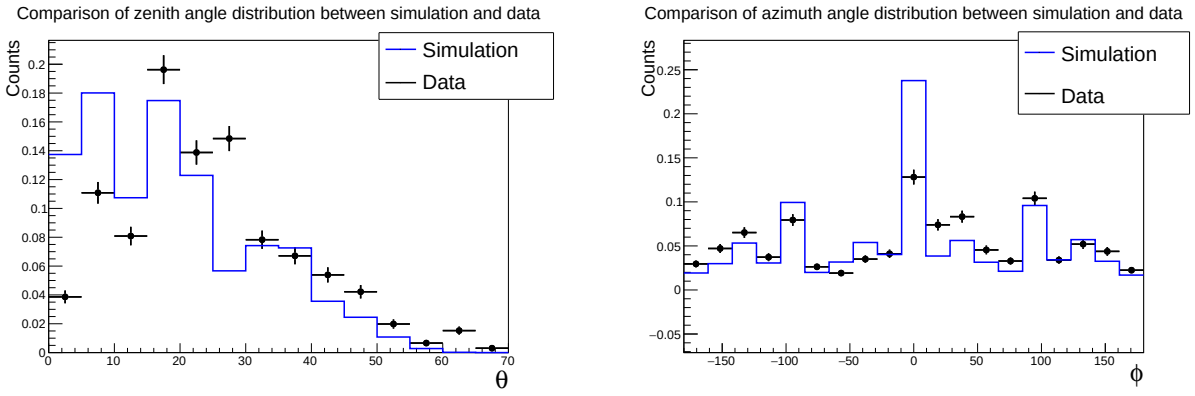

(a) Zenith angle comparison

(b) Azimuth angle comparison

Figure 4.3: Comparison of reconstructed angles for real and simulated data. No spacers configuration.

translator.cpp has also been created to convert decimal files to binary files to double-check the reconstructed angles. Each event corresponds to 16 bytes : 8 for the hits related to a total of 64 strips and 8 for the time stamp). If the bit equals 1, the strip is touched.

4.2 Misalignment

Misalignment of detectors can have a significant impact on track reconstruction. This problem has been raised by Dr. Cristina Cârloganu who is PI of the TOMUVOL collaboration that is showing the feasibility of muographic imaging of volcanoes with the studies conducted on Puy de Dôme with muons [1].

This section is thus a little demonstration of the effect of misalignment on the distribution of residuals obtained from reconstructed angles through a simulation that have been written for the purpose.

For that, CSV output file (x_0, y_1, x_2, y_3) from the previous simulation were re-used and *amplitudeCalculator.cpp* was adapted to take into account the displacement of the detectors.

Let Δ be a uniform random value in a specified range that stands for the displacement of an entire detector, e.g. $\Delta = 0.5cm$ means that all the strips will be displaced of 0.5 cm compared to their initial position. Following this definition, four Δ's (for the four chambers) are randomly generated : $\Delta_0; \Delta_1; \Delta_2; \Delta_3$ and we look at the difference between misaligned and aligned configurations of the chambers. Fig. 4.4 shows some examples of misalignment studies. For

small displacement of detectors between -1cm and 1 cm, it can lead to a standard deviation of $\sim 8°$ in θ and of $\sim 40°$ in ϕ. This would immediately lower the spatial and angular resolution of the equipment and thus for example, muography studies would be impossible.

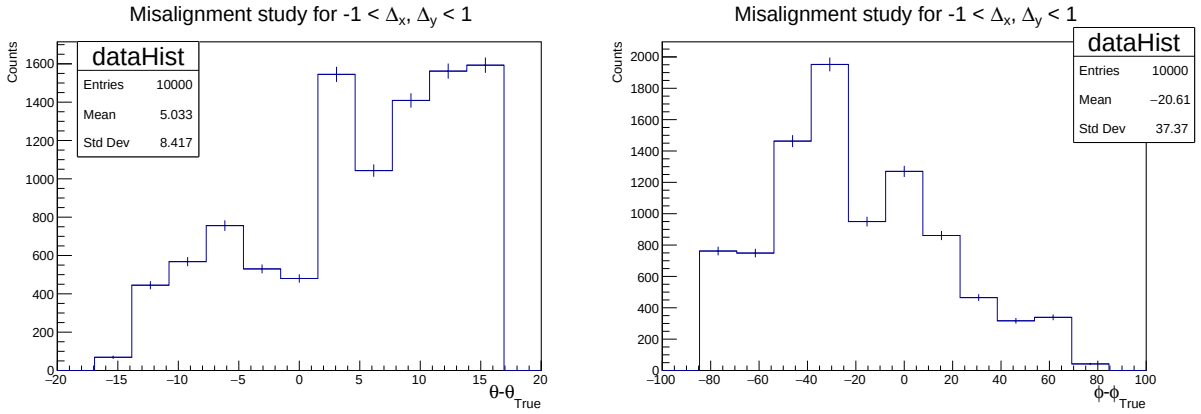

(a) Bias in zenith angle

(b) Bias in azimuth angle

Figure 4.4: Bias introduced due to misalignment of detectors : $\Delta_0 = 0.75cm; \Delta_1 = -0.96cm; \Delta_2 = -0.47cm; \Delta_3 = 0.64cm$

Some other plots with various deltas are shown in Appendix 4.

As a result, precise alignment of detectors is needed for the track reconstruction otherwise one can obtain large biases.

4.3 Acceptance versus angular resolution

This section is dealing with the compromise that could be found to reach acceptable acceptance and angular resolution.

For the calculations, the acceptance of the detectors has been defined as follows :

Acceptance : ratio between the number of muons crossing one detector and the number of muons crossing the three others left.

Among muons crossing detector A, how many muons would cross the three others ?

Wheras, the angular resolution is the precision with which we reproduce the position hit in each chamber. This is illustrated in fig. 4.5.

Angular resolution : using the small-angle approximation, we define :

$$\sigma_\theta \simeq tan\sigma_\theta \equiv \frac{\Delta x}{W}, \tag{4.2}$$

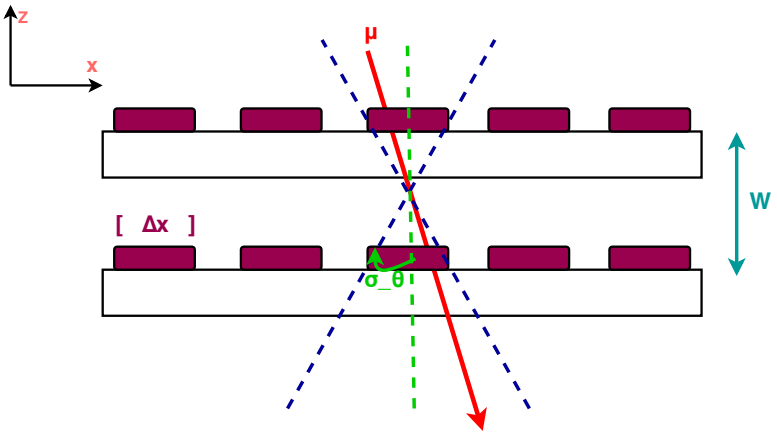

Figure 4.5: Angular resolution in plan x-z

where, Δx is the strip width and W the distance between x(or y)-detectors.

Using the simulation made in section 4.1., the behaviour of these two variables has been studied by modifying the parameter w. Fig. 4.6 shows the final compromise. There is a trade-off between the ascending angular resolution and the descending acceptance to keep a large acceptance of muons while getting a high angular resolution that is more than necessary for muography studies (cfg. section 1.4).

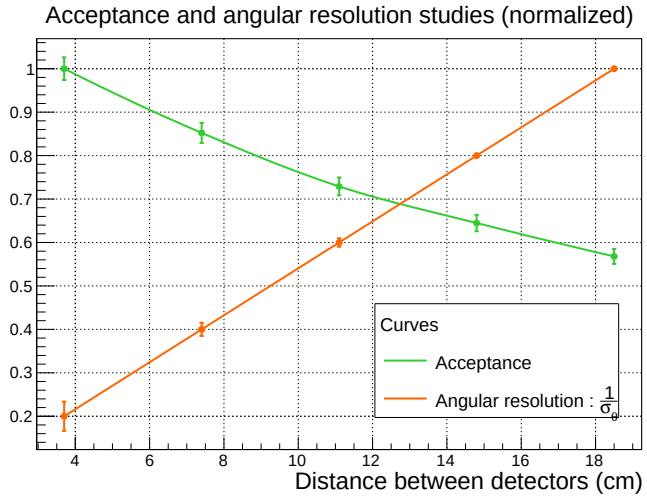

Figure 4.6: Acceptance versus angular resolution for different w-values.

4.4 Signal induced

The following simulation has been made in order to calculate the signal expected in one of the chambers built.

Fig. 4.7a & 4.7b shows the induced current versus time for electrons, ions and the total according to the Shockley-Ramo theorem (cfg. section 2.2) whereas, fig. 4.7c shows the same plot but with the formula obtained from the extension of Ramo's theorem. The assumptions used are the following :

1. Parallel plate geometry with 2-mm gap filled with argon
2. 1000 layers inside the gap (10^{-6}cm thick)
3. Primary ion pairs created : $n_{eff} = \frac{dE/dx}{w_{Ar}} = 93.84 ip/cm$
4. Electron speed : $v_e = 10^4$m/s
   Ion speed : $v_i = 10^3$m/s (this is not the real value, ions are slower)
5. Towsend coefficient : $\alpha \sim 3.5[1/cm]$
6. Attachement coefficient : $\beta \sim 4.5[1/cm]$
7. Glass relative permittivity $\epsilon_{r_1} = 5$
8. Argon gas relative permittivity $\epsilon_{r_2} = 1.000052$
9. Vacuum permittivity $\epsilon_0 = 8.85 \cdot 10^{-12}$F/m
10. Glass thickness : 1.1 mm

The difference obtained between the basic theorem and extended Ramo's theorem is not obvious but it exists as these plots can demonstrate (factor ~ 1.28). The main difference comes from the multiplication factor (Townsend coefficient) that multiply the signal of a factor 1000.

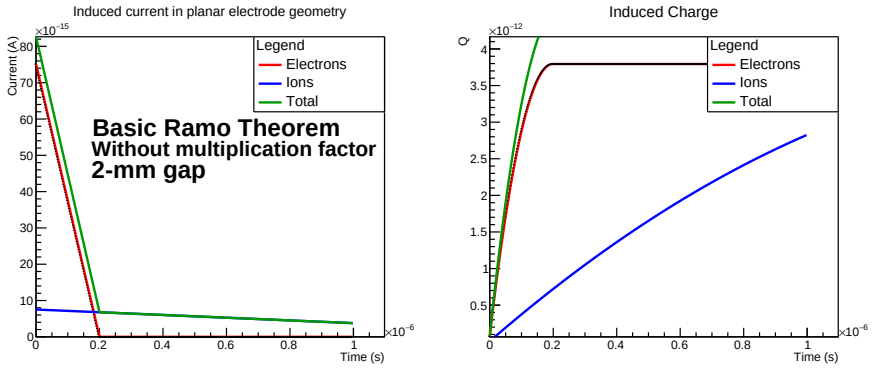

(a) Signal induced without multiplication factor

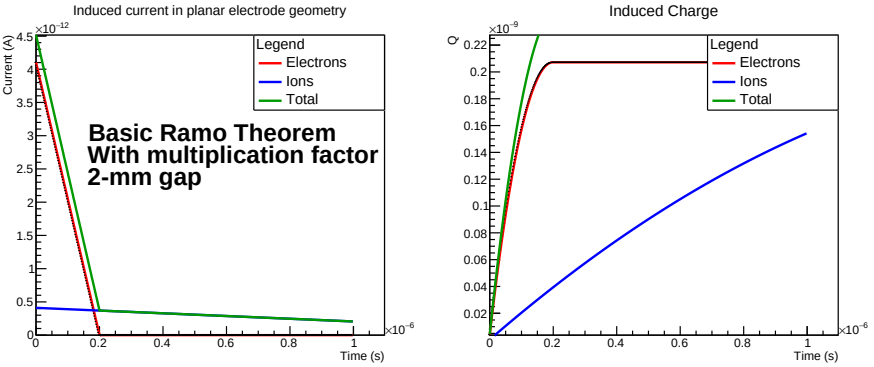

(b) Signal induced with multiplication factor

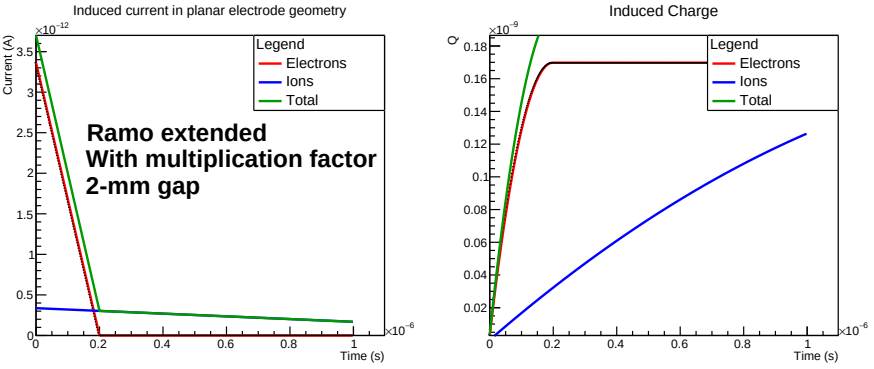

(c) Signal induced with multiplication factor - Extended Ramo theorem

Figure 4.7: Comparison of signals induced in parallel plate geometry of 2-mm gap according to Shockley-Ramo theorem (non)-extended

This analysis has been presented for a 2-mm gap because it was the glaring one to demonstrate the differences that exist between both forms of the Ramo's theorem. Simulation for 1-mm gap has been added to appendix 4.

This chapter was dedicated to simulation. We tested some geometric features of our setup like the misalignment, acceptance and angular resolution of the detectors. It allows us to compare with our real data and it seems compatible. In addition, it showed us the optimal trade-off between acceptance and angular resolution. The signal induced in RPCs was also studied to give us an idea of how big the signal would be. As a result, the signal obtained is very small (10^{-12}A), therefore amplifiers have to be chosen with care.

To improve the performance of our muon telescope, upgrades are needed. In its actual state, it could not be used for muographic studies. The next chapter will then be dedicated to the upgrading.

CHAPTER 5

Future and prospects

This chapter is dedicated to the possible upgrades of the muon telescope that could be undertaken in the future. It is focused on the electronic part given that the actual readout system is very noisy and would not be suited for muography studies. The end of the chapter deals with the potential studies that could be led in the context of muography with such a telescope.

5.1 Readout system

In this section, several possibilities for a future readout system are investigated. For the moment as explained in section 3.1, the front-end electronics used is an ASIC called "CMS RPC front-end electronics" [59], containing both the amplifier and pulse shaping for digital signal output. However, these CMS front-end are very noisy and are now 18 years old. Moreover, the documentation on them is very poor, thus a more recent electronic technology would be more than welcome. In addition, in an ideal future, the goal is to have much more strips than today to increase the spatial resolution that is required to image structures. Henceforth, large number of strips means large number of channels. The challenge is then to reduce the size of the required electronics at most.

5.1.1 Multiplexing

The first solution found is multiplexing, which is basically a method that integrates multiple analog or digital signals into a single, complex signal over a shared medium.

A method that may be appropriate for our setup is called *Genetic Multiplexing* that has been established in 2012 by Sebastien Procureur's team at SACLAY [67].

1. **Working principle**

   The main goal is to read a very large number of strips with as few channels as possible.

   It is based on the fact that if the width of the strips is such that at least two consecutive strips record a signal from the passage of a particle, and if it is unlikely to have two particles passing simultaneously, the redundancy can be exploited to compress the information in an unambiguous way.

   Thus this redundancy is used to combine channels with strips in such a way that two given channels are connected to neighbouring strips only once in the detector as shown in figure 5.1.

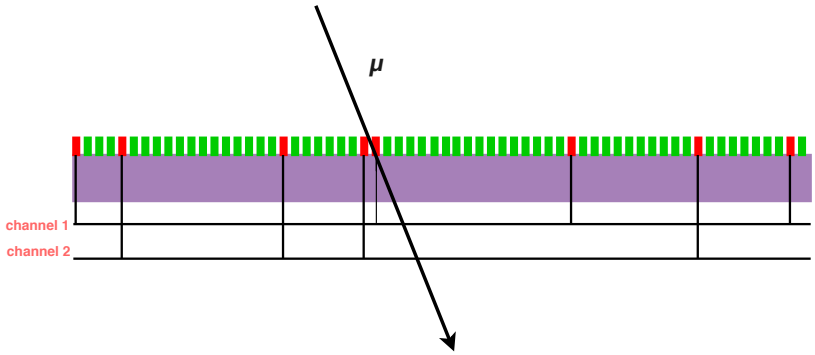

Figure 5.1: Illustration of genetic multiplexing for two channels.

The sequence of channels uniquely codes the muon position in the detector.

More practically, we represent the relation between n channels and p strips by a p list of channel numbers. Therefore, for n channels, there are a priori $\frac{n(n-1)}{2}$ unordered doublets combinations. This implies that the detector should be equipped with at most $p = \frac{n(n-1)}{2} + 1$ strips.

Depending on the incident particle flux, the degree of multiplexing can be easily adapted by following this method.

2. **Recent applications**

   The 1st prototype (1D) was a Micro-Pattern Gaseous Detector (MPGD). These are widely used in particle physics for their excellent track and detection capabilities. It has 50x50cm^2 active area that reads n = 61 channels for p = 1024 strips (with a 488 micron pitch)!

   It demonstrated that the principle works with $\sim 90\%$ average efficiency.

   Their 2nd protoype was basically the same except that they used resistive strips to improve the gain and robustness. The readout was made with two connectors to obtain 2D results (X and Y). In this way, it worked at full efficiency.

The main advantage is that the size of the electronics is reduced. In addition, the large production capability is also an asset. The drawbacks of this technique are its expensive price and the fact that it would lead to several months of work.

5.1.2 HardRoc chip

Another solution that could be done is to use a HAdronic Rpc Detector ReadOut Chip (HARDROC) instead of two CMS front-ends [68]. There are 10 years of developments between these two technologies. In addition, the documentation of these chips is complete and richer than the ones found for CMS front-ends[1].

HARDROCK is a 64-channel front-end ASIC designed to readout negative fast (< 1ns) and short (< 10ns) current pulses with tunable thresholds. This chip would answer to the stringent electronics requirements we would like : hundreds (or millions) of channels have to be read out. Chips can be embedded inside the detector without any external circuitry, it's all in there.

It provides a readout with three thresholds set by three integrated 10-bit DACs and tunable between 10 fC up to 10 pC. The real values of thresholds are not arbitrary in this case, we know them and can interpret them physically. There is also the gain that can be tuned individually for each channel to maximize the uniformity between the 64 channels. Each channel is an independent trigger and auto-trigger down to 10 fC and up to 10 pC.

Finally, its price is affordable (500€) for one chip. That means, $8000eur$ for 1000 channels.

5.2 Construction

Some part of the construction of the telescope need to be replaced or tested because the techniques used were not successful.

[1] `https://www.weeroc.com/fr/products/hardroc-3b`

5.2.1 Resistive coating

The first thing that needs to be changed is the resistive coating (see Section 3.1.1).

The paint mixture used makes deposits in the containers when we mix it with methanol. As a result, when it is applied on glass plates, there are some clumps that badly affect the painting uniformity. Bad painting uniformity means non-uniform electric field that leads to a difficult recharge after an ionizing event (see section 2.7.1) and a reduced detection efficiency.

In addition, the actual painting method uses a roller to apply the coating but it is still difficult to ensure uniformity with this technique recommended by experts from University of Ghent. Given that the roller is narrower than the active area that needs to be painted, some marks are persistant from the edges of the roller.

A solution could be to buy a new bottle of paint given that the one we got was potentially poor made at the manufacturer facility.

Otherwise, another solution would be to change our resistive coating for a conductive paper or graphite layer that are mostly used with this type of detectors.

5.2.2 Gap width

Our actual gap width is 1.1mm. It is done with edge spacers in PEEK material.

Since it is very narrow for a gap with very thin glass plates (1.1mm), we have some concerns about the bending in the middle that could cause an electrostatic attraction between the plates and lead to a non-uniform electric field.

A possible solution to these problems would be to add spacer balls[2]($\rho = 10^{15}\Omega m$ and dielectric strength = 11.4 kV/mm) that are glued to prevent the bending [48] [35] and enlarge the gap to prevent electrostatic attraction from the high voltage difference. However, the spacer balls have some drawbacks since they blind the detectors when they are placed above strips. One has to be careful with the spacer positions.

5.3 Muography studies

This section aims at showing muography applications that could be feasible with our muon telescope developed at UCL.

Since it is relatively small, it would be inconvenient for active volcanoes studies that need large-area detectors (large statistics and spatial dispersion of muons much important). How-

[2]Grade 5 ZrO_2 ceramic precision balls from Sceram (10 Chemin des Rosiéristes 69410 Champagne-au-Mont-d'Or, France)

ever, its has several assets that still makes it an attractive choice with respect to other detectors previously employed for imaging on smaller scales.

As a matter of fact, its compact size, its portability and its gas-tightness features solve the usual safety and logistic issues for gas detectors operated underground and/or inside small rooms. Thus we could optimize it for the operating conditions that one could find in archaeological and nuclear applications. Another strength of our telescope is its versatility. Indeed, it could image either in absorption mode or in scattering mode since it is in detached pieces, i.e we can position objects between the detectors or keep them aligned in front of the object to image.

Examples of feasible applications :

- **Archaelogy**

  As the ScanPyramids project has already desmonstrated [6], it is possible to image rooms inside a pyramid thanks to high-resolution muography. During their mission in 2017, they discovered the "ScanPyramids Big void" in the Khufu's Pyramid in Egypt. Their detectors were placed outside because they were large and needed a continuous gas flushing system with provided gas bottles. Our telescope doesn't have these limitations since it is a sealed and gas-tight system. We could therefore use it to image chambers in a pyramid by directly placing it inside and below the suspected void.

  Pyramids are not the only archeological structures where muon imaging can be performed. For example, the void inside structure of other large man-made constructions can also be infered.

- **Underground mapping**

  If we want to image an underground structure (mines, galleries, caves, overburden over a tunnel,...), the muon detector has to be located below the target of interest. In order to proceed to the detector placement, we have two possibilities : tunnels or boreholes.

  The constraint here is then the diameter of the underground tunnel or borehole. It has to be larger than a few meters for large-area detectors. In addition to limited space, the instrument should cope with potential vibrations or shocks during its insertion. Ours would perfectly avoid these problems. However, it would not be convenient if boreholes are needed given that they are narrow shafts drilled in the ground in a round shape, i.e rod type muon detector would be required.

  Several experiments have already been conducted in order to find ore in existing mines. Their primer goal is to make the detection of heavy materials (uranium, gold or lead) easier.

  Another example is the natural laboratory of Mt. Echia, in Naples (Italy). Cavities created by digging in the yellow tuff of Mt. Echia were imaged by a muon tracker installed at two different positions under a tuff thickness of about 40m [9].

Beyond ore detection, the whole field of geoscience could benefit from this new class of underground instruments, to study the hydrology of soils, geological shells, faults, or perhaps one day to monitor deep storage sites like the ones for CO_2.

- **Nuclear waste monitoring**

  The muon sensitivity to high-Z material has already been investigated for several years with the characterization of nuclear waste making it well-kwown through muography science and close to market entry. For example, *Lynkeos Technology Ltd*[3] is the first company in the UK to commercialize a muography system for nuclear waste characterization. Fig. 5.2 shows an illustration of the application.

Figure 5.2: Muon tomography used to characterize nuclear waste in containers.

Our detector could be optimized to image the contents of a nuclear waste container and characterize any residual nuclear materials stored within. We just have to place two detectors above and two under the active waste drum.

This final chapter presented the future upgrades that could be done in order to improve the performance of the muon telescope. We mainly discussed about the electronics part of the system that need to be modified with either multiplexing or a new chip. Our current readout system is too noisy. The resistive coating and gap width could also revised since we had some issues with them. Finally, some realistic applications in muography that could be conducted with our muon telescope in the future were presented.

[3] https://www.lynkeos.co.uk/

Conclusion

This work had as a main goal the development of a muon telescope based on four mini-glass Resistive Plate Chambers that would be compact, portable and gas-tight. This part was successful and led to data collection and analysis.

Several campaigns have been conducted in particular in the Utah Desert (USA) at the Mars Desert Research Station in the context of the "UCL to Mars 2018" mission. It demonstrated the deficiencies of our apparatus that had to be resolved before the second-data taking campaign. After having changed the polarity of high voltage and gas mixture of the detector, we could observe the first muons events at UCL.

We could then start the data analysis part that firstly consisted in finding the operating high voltage and thresholds. After this step, muon track reconstruction could be undertaken showing the distribution of the cosmic muons.

In parallel, simulation tests have been performed to study the acceptance and angular resolution of the telescope. The effect of misalignement of the four chambers was also investigated. In additon, a small simulation to calculate the signal induced in such a detector was carried out.

Regarding its future, after some upgrades (mostly at the electronic level), this muon telescope could be perfectly optimized for muon imaging by using the so-called *muography* techniques that are on the rise since fifteen years. The interesting targets seem to be mainly found in archaelogy and in nuclear applications for our kind of detector. We would enter in the growing community of muographers coming from all over the world, profit from their expertise and create new collaborations.

Bibliography

[1] A. Portal et al., "Inner structure of the puy de dôme volcano: cross-comparison of geophysical models (ert, gravimetry, muon imaging)," *Geosci.Instrum.Method. Data Syst.* **2** no. 47, (2013) .

[2] S. Chatrchyan et al., "The CMS experiment at the CERN LHC." doi:10.1088/1748-0221/3/08/S08004, 3:s08004, 2008. [Journal of Instr.].

[3] The CALICE Collaboration, "First results of the CALICE SDHCAL technological prototype," *Journal of Instrumentation* **11** (Apr., 2016) P04001, arXiv:1602.02276 [physics.ins-det].

[4] Seth H. Neddermeyer and Carl D. Anderson, "Note on the nature of cosmic-ray particles," *Phys. Rev.* **51** no. 884, (1937) .

[5] E.P. George, "Cosmic rays measure overburden of tunnel," *Comm. Eng.* no. 455, (1955) .

[6] L. W. Alvarez and al., "Search for hidden chambers in the pyramids," *Science (New York, N.Y.)* **167** (03, 1970) 832–9.

[7] H.Tanaka et al., "High resolution imaging in the inhomogeneous crust with cosmic-ray muon radiography: The density structure below the volcanic crater floor of mt. asama, japan," *Earth and Planetary Science Letters* **263** no. 104, (2007) .

[8] The ScanPyramids mission, "Discovery of a big void in khufu's pyramid by observation of cosmic-ray muons." http://dx.doi.org/10.1038/nature24647, December, 2017. see also www.scanpyramids.org/.

[9] G. Saracino et al., "Imaging of underground cavities with cosmic-ray muons from observations at mt. echia (naples)," *Scientific Reports* **11** no. 1181, (2017) .

[10] H. Gomez, C. Carloganu, D. Gibert et al., "Studies on muon tomography for archaeological internal structures scanning," *Journal of Physics: Conference Series* **718** no. 5, (2016) 052016. http://stacks.iop.org/1742-6596/718/i=5/a=052016.

[11] F. Ambrosino et al., "Assessing the feasibility of interrogating nuclear waste storage silos using cosmic-ray muons," *Journal of Instrumentation* **10** (June, 2015) T06005, arXiv:1411.2382 [physics.ins-det].

[12] C. Patrignani et al. (Particle Data Group, "Summary tables," *Chin. Phys. C* **40** no. 100001, (2016 and 2017 update) .

[13] Coulomb, C. A. , *Mémoires sur l'électricité et le magnétisme.* Paris : Chez Bachelier, 1789. https://archive.org/details/mmoiressurllectr00coul.

[14] T. Wulf, "Observations on the radiation of high penetration power on the eiffel tower," *Physikalische Zeitschrift* **11** (1910) 811.

[15] V. Hess *Phys. Zeit.* **13** (1912) 1084.

[16] D. Pacini, "La radiazione penetrante alla superficie ed in seno alle acque," *Nuovo Cim* **VI/ 3** (1912) 93.

[17] Millikan and Cameron, "Origin," *Phys. Rev.* **32** (1928) 534.

[18] A.H. Compton *Phys. Rev.* **43** (1933) 387.

[19] B. Rossi *Phys. Rev.* **36** (1930) 606.

[20] L. Alvarez and A.H. Compton *Phys. Rev.* **43** (1933) 835.

[21] C. Patrignani et al. (Particle Data Group), "Cosmic rays," *Chin. Phys. C* **40** (2017) 100001.

[22] M. Tanabashi et al. , "Particle data group," *Phys. Rev. D* **98** (2018) 030001.

[23] P. Shukla, "Energy and angular distributions of atmospheric muons at the Earth," *ArXiv e-prints* (June, 2016) , arXiv:1606.06907 [hep-ph].

[24] T. K. Gaisser *Astropart. Phys.* **16** (2002) 285.

[25] T. K. Gaisser, "Cosmic rays and particle physics," *Cambridge University Press* (1990) .

[26] S. Procureur, "Muon imaging: Principles, technologies and applications," *Nucl. Inst. Meth. in Phys. A* **878** (2018) 169 – 179. http://www.sciencedirect.com/science/article/pii/S0168900217308495. Radiation Imaging Techniques and Applications.

[27] E. Cortina Gil, "Interaction radiation-matter," *LPHY2236 (UCL)* **Chapter 2** (2012) .

[28] A. Bettini, *Introduction to Elementary Particle Physics*. Cambridge University Press, 2008. https://books.google.be/books?id=HNcQ_EiuTxcC.

[29] D.E Groom et al, "Muon stopping power and range," *Atomic Data and Nuclear Data Tables* **76** no. 2, (2001) .

[30] David F. Mahon, "Characterizating encapsulated nuclear waste using cosmic-ray muon tomography." http://player.slideplayer.com/35/10386516/#, 2015.

[31] R. Santonico and R. Cardarelli, "Development of resistive plate counters," *Nucl. Instrum. Meth* (1981) 377–380.

[32] G. Aad et al., "The ATLAS experiment at the CERN large hadron collider." doi:10.1088/1748-0221/3/08/S08003, 3:s08003, 2008. [Journal of Instr.].

[33] Yi-Fang Wang, "The BES-III experiment at the high luminosity tau-charm factory." https://arxiv.org/pdf/0711.4199.pdf, September, 2007. [Institute of High Energy Physics, Beijing, China].

[34] Jarne De Clercq, "Characterization of a glass resistive plate chamber for a future upgrade of the CERN CMS experiment," *Faculteit Wetenschappen Vakgroep Fysica en Sterrenkunde, Universiteit Gent* (2015) .

[35] Dieter Loterman, "Development of a glass resistive plate chamber for the phase-2 upgrade of the CMS detector at the Large Hadron Collider," *Faculteit Wetenschappen Vakgroep Fysica en Sterrenkunde, Universiteit Gent* (2014) .

[36] I. Laktineh , "Novel gaseous detectors and applications," *Université Lyon1, France* (2017) .

[37] R. Cardarelli et al, "Avalanche and streamer mode operation of resistive plate chambers," *Nucl. Instrum. Meth A* **382.3** (1996) 470–474.

[38] G. E. Knoll, "Radiation detection and measurement," *University of Michigan* (1999) 789–794.

[39] C. Lu, "Induced signal in RPC," *SNIC Symposium* (2006) 11.

[40] W. Riegler, "Extended theorems for signal induction in particle detectors vci 2004," *Nucl. Instr. Meth A* **535** no. 1, (2004) 287 – 293. http://www.sciencedirect.com/science/article/pii/S0168900204016560. Proceedings of the 10th International Vienna Conference on Instrumentation.

[41] W. Riegler, "Induced signals in resistive plate chambers," *Nucl. Instr. Meth. A* **491** (09, 2002) 258–271.

[42] T. Heubrandtner, B. Schnizer, C. Lippmann, and W. Riegler, "Static electric fields in an infinite plane condenser with one or three homogeneous layers," *Nucl. Instr. Meth. A* **489** no. 1, (2002) 439 – 443. http://www.sciencedirect.com/science/article/pii/S0168900202008057.

[43] G. Carboni et al , "Final results from an extensive ageing test of bakelite resistive plate chambers," *Nucl. Instr. Meth. A* **51** no. 5, (2004) .

[44] M. Morales et al , "Conductivity and chage depletion ageing of resistive lectrodes for high rate rpcs," *Journal of Instrumentation* **8** no. 01, (2013) P01022. http://stacks.iop.org/1748-0221/8/i=01/a=P01022.

[45] J. Va'vra, "Attempt to correlate the ionic model with observations in BaBar RPC chambers and R&D tests," *IEEE Transactions on Nuclear Science* **51** no. 5, (2004) 2145–2150.

[46] H. Czyrkowski et al , "New developments on resistive plate chambers for high rate operation," *Nucl. Instr. Meth. A* **419** (1998) 490–496.

[47] G. Battistoni et al, "Resistive cathode transparency," *Nucl. Instr. Meth.* **202** no. 3, (1982) 459 – 464. http://www.sciencedirect.com/science/article/pii/0167508782905403.

[48] Sander Vanheule, "Design of a glass resistive plate chamber for the upgrade of the compact muon solenoid muon system," *Faculteit Wetenschappen Vakgroep Fysica en Sterrenkunde, Universiteit Gent* (2013) .

[49] G. Iaselli et al , "Properties of $C_2H_2F_4$-based gas mixture for avalanche mode operation of resistive plate chambers," *Nucl. Instr. Meth. A* **398** (1997) 173–179.

[50] P. Paulocini, "Test of different gas mixtures for RPC detectors," *Nucl. Instr. Meth. A* **369** (1997) .

[51] A. Yamaguchi et al, "Performance of glass rpc operated in streamer mode with SF_6 mixture," *Nucl. Instr. Meth. A* **455** (2000) 397–404.

[52] M. Abbrescia et al, "Eco-friendly gas mixtures for resistive plate chambers based on tetrafluoropropene and helium," *Journal of Instrumentation* **11** no. 08, (2016) P08019. http://stacks.iop.org/1748-0221/11/i=08/a=P08019.

[53] J. Datta et al, "Qualification of eco-friendly gas mixture for avalanche mode operation of RPC,".

[54] M. Abbrescia *et al.*, "The simulation of resistive plate chambers in avalanche mode: Charge spectra and efficiency," *Nucl. Instrum. Meth.* **A431** (1999) 413–427.

[55] I. Crotty et al, "The wide gap resistive plate chamber," *Nucl. Instr. Meth. A* **360** no. 3, (1995) 512 – 520. http://www.sciencedirect.com/science/article/pii/0168900295000399.

[56] CMS Collaboration, "Calibration of the RPC working voltage in the CMS experiment," Tech. Rep. CMS-CR-2012-055, CERN, Geneva, Apr, 2012. https://cds.cern.ch/record/1457409.

[57] C. Gustavino, "Performance of glass RPC operated in avalanche mode," *Nucl. Instr. Meth. A* **527** (July, 2004) 471–477.

[58] W. Riegler, C. Lippmann and R. Veenhof, "Detector physics and simulation of resistive plate chambers," *Nucl. Instr. Meth. A* **500** (2003) 144–162.

[59] Abbrescia, M. ; Bruno, Giacomo Luca ; et. al, "New developments on front-end electronics for the CMS resistive plate chambers," *Nucl. Instr. Meth. A* **456** no. 1-2, (2000) 143–149.

[60] F. Loddo, "CMS RPC front end board endcap version," *INFN-BARI* .

[61] Analog Device, "10-bit digital temperature sensor (ad7416) and four single-channel adcs." www.analog.com, 1998–2010.

[62] Analog Device, "2.5 v to 5.5 v, 400 μa, 2-wire interface, quad voltage output, 8-/10-/12-bit dacs." www.analog.com, 2005.

[63] Iseg Spezialelektronik GmbH / Germany, "Dps series : High precision built-in or system capable high voltage power supply module." www.iseg-hv.com, 2017.

[64] Texas Instruments, "PCF8574 remote 8-bit I/O expander for I²C bus." www.ti.com, JULY 2001 – REVISED MARCH 2015.

[65] Analog Device, "8-channel, 12-bit, configurable adc/dac with on-chip reference, i 2 c interface." www.analog.com, 2014-2017.

[66] S. Wuyckens, "Muoscope user guide." http://github.com/sowuy/User-Guide, 2018.

[67] S. Procureur, R. Dupré, and S. Aune, "Genetic multiplexing and first results with a 50×50cm2 micromegas," *Nucl. Instr. Meth. A* **729** (2013) 888 – 894. http://www.sciencedirect.com/science/article/pii/S0168900213012126.

[68] S. Callier, F. Dulucq, C. de La Taille, N. Martin-Chassard, and N. Seguin-Moreau, "HARDROC, Readout chip of the Digital Hadronic Calorimeter of ILC," in *Proceedings, Topical Workshop on Electronics for Particle Physics (TWEPP09)*, CERN. CERN, 2009. http://inspirehep.net/record/1658837/files/p122.pdf.

Appendices

Appendix .1: Shockley-Ramo theorem demonstration

The equation (2.1) can be obtained very easily by using the second formula of the Green theorem. Let's derive it :

We need a set of electrodes a charge q and a tiny equipotential sphere. First we put the potential of all the electrodes to zero. The potential of the sphere is put to V_q. Let V be the potential of the electrostatic field in the region between the electrodes and the sphere. we have,

$$\nabla^2 V = 0 \tag{1}$$

Then we apply Gauss law on the sphere and get :

$$\int_{\text{sphere}} -\frac{dV}{dn} dS = \frac{q}{\epsilon_0} \tag{2}$$

Let us do the same calculation but by taking away the charge and putting the electrode A to a potential unit $V_{A=1}$. We call the electrostatic potential V_1. In that case, we have,

$$\nabla^2 V_1 = 0 \tag{3}$$

$$\int_{\text{sphere}} -\frac{dV_1}{dn} dS = 0 \tag{4}$$

Finally by applying the Green theorem with the right boundaries:

$$\int_{\text{volume}} (V_1 \nabla^2 V dV - V \nabla^2 V_1) dv = \int_{\text{surface}} (V_1 \frac{\partial V}{dn} - V \frac{\partial V_1}{dn}) ds \tag{5}$$

Obviously, the left term is null. The right term of the equation has 3 contributions :

1. A null contribution from the surface of all the other electrodes except A
2. The contribution on A gives : $\int 1 \frac{\partial V}{dn} = -\frac{Q_A}{\epsilon_0}$
3. The contribution on the surface sphere gives : $\int -V_q \frac{\partial V}{dn} = -\frac{q}{\epsilon_0} V_q$

By equalizing the two last expressions, we find the Shockley-Ramo theorem as expected :

$$Q_A = -qV_q \tag{6}$$

$$i_A = \frac{dQ_A}{dt} = -q\frac{dV_q}{dt} = -q\frac{dV_q}{dl} dl = q \overrightarrow{v} \cdot \overrightarrow{E_w} \tag{7}$$

Appendix .2: Extended Shockley-Ramo theorem demonstration

To extent the Shockley-Ramo theorem to resistive plate chambers, W. Riegler uses the quasistatic approximation of Maxwell's equations [40] [41].

First, let's take the Poisson equation for a charge density :

$$\rho(\vec{r}, t) = \rho(\vec{r}) \delta(t) \tag{8}$$

$$\text{(Laplace domain)} \qquad \vec{\nabla} \left[\epsilon(\vec{r}, s) \vec{\nabla} \right] \Phi(\vec{r}, s) = -\rho(\vec{r}, s) \tag{9}$$

A solution of the Poisson equation for a homogeneous medium ($\rho(\vec{r}) = \delta(\vec{r})$) is the Green's function $G(\vec{r}) = \frac{1}{4\pi\epsilon|\vec{r}|}$.

By replacing $\epsilon(\vec{r}, s)$ with $\epsilon(\vec{r}, s) + \frac{1}{s}\sigma(\vec{r}, s)$ and performing a inverse Laplace transform, we get :

$$G(\vec{r}, t) = \frac{1}{4\pi\epsilon \left|\vec{r}\right|} \left(\delta - \frac{1}{\tau} e^{-t/\tau} \right) \tag{10}$$

where $\tau = \frac{\epsilon}{\sigma}$.

If we put a charge density $\rho(\vec{r})$ at time t=0 into the medium i.e $\rho_e(\vec{r},t) = \rho(\vec{r})\Theta(t)$, we can write the time-dependant potential as

$$\Phi(\vec{r},t) = \frac{e^{-t/\tau}}{4\pi\epsilon}\int_V \frac{\rho(\vec{r'})}{\left|\vec{r}-\vec{r'}\right|}d^3r' \tag{11}$$

and we can derive the induced current with the Green theorem. Now let's apply the same reasoning to our case where the electrodes are embedded in a medium with $\epsilon(\vec{r},s)$ and $\sigma(\vec{r},s)$.

Now we take away the charge and put the electrodes at fixed tensions, we have $V_i(s) = \Phi(\vec{r},s)\mid_{\vec{r}=S_i}$ with S_i the surface of electrode i.

The expected charges on the electrode surfaces and current are given by

$$Q_i(s) = \int_{s_i} \epsilon(\vec{r},s)\frac{\partial\Phi(\vec{r},s)}{\partial n}dS \tag{12}$$

$$I_i(s) = \int_{s_i} \sigma(\vec{r},s)\frac{\partial\Phi(\vec{r},s)}{\partial n}dS \tag{13}$$

Both terms are related by the following equation if the electrodes are connected to an external current source :

$$sQ_i(s) + I_i = I_i^{ext} \tag{14}$$

where,

With $f(\vec{r},s) = \epsilon(\vec{r},s)$, we solve the following generalized Green theorem for the boundery surface S:

$$\begin{aligned}\int_V \left[\Psi(\vec{r})\vec{\nabla}(f(\vec{r})\vec{\nabla})\Phi(\vec{r}) - \Phi(\vec{r})\vec{\nabla}(f(\vec{r})\vec{\nabla})\Psi(\vec{r})\right]dV = \\ \int_S \left[\Psi(\vec{r})f(\vec{r})\frac{\partial\Phi(\vec{r})}{\partial n} - \Phi(\vec{r})f(\vec{r})\frac{\partial\Psi(\vec{r})}{\partial n}\right]d\vec{A}\end{aligned} \tag{15}$$

where,

$\Phi(\vec{r},s)$: potential function in the presence of a charge

$\Psi_V(\vec{r},s)(\Psi_I(\vec{r},s))$: potential function with charge removed but with floating (grounded) electrodes = "weighting potential".

With some further calculations, one can find the voltages and currents induced on the electrodes by a time varying charge density :

$$V(t) = \frac{1}{q_0} \int_0^t \int_V \Psi_V(\vec{r'}, t - t') \frac{\partial \rho_e(\vec{r'}, t')}{\partial t'} d^3r' dt' \tag{16}$$

$$I(t) = \frac{1}{V_0} \int_0^t \int_V \Psi_I(\vec{r'}, t - t') \frac{\partial (\rho_e \vec{r'}, t')}{\partial t'} d^3r' dt' \tag{17}$$

These are the both desired theorem for this extension of Ramo's theorem.

Appendix .3: Data analysis RUN2 - additional plots

Appendix .3.1: Hits pattern

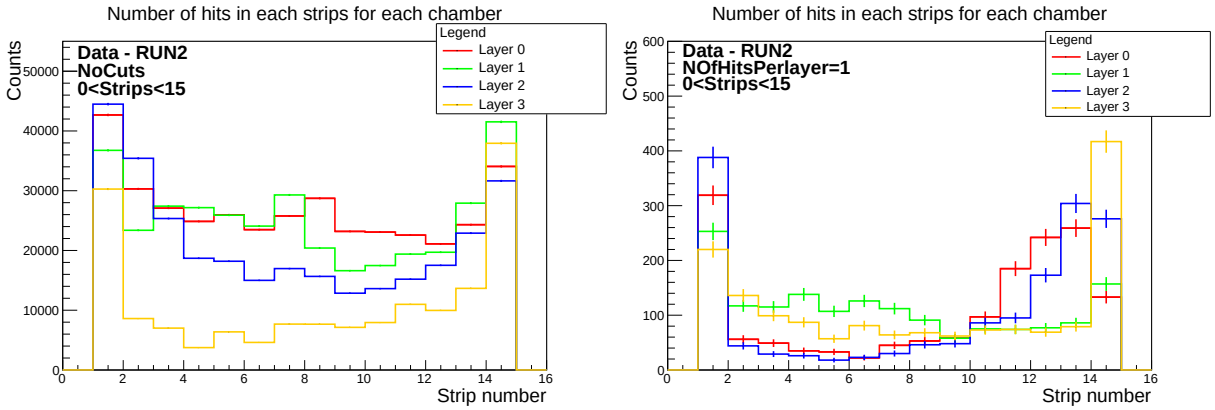

(a) No cuts

(b) Number of hits per layer equal to one

Figure 3: Hits pattern of RUN2 with strip 0 and 15 excluded

Appendix .3.2: Angles reconstructed

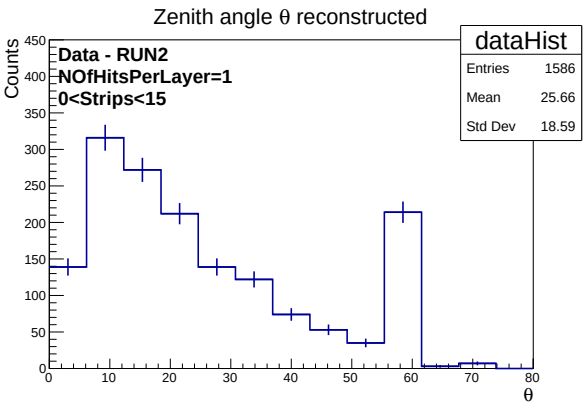

(a) Zenith angle with strip 0 and 15 excluded

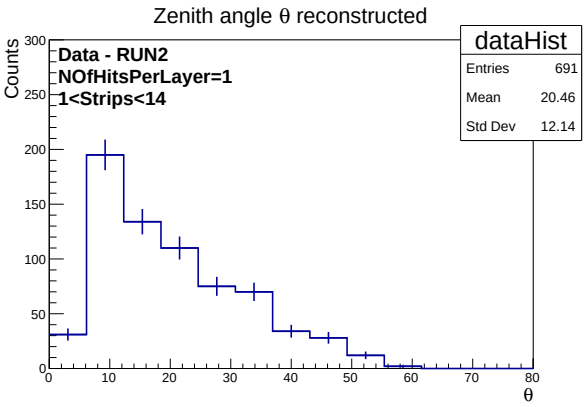

(b) Zenith angle with strip 0, 1, 14 and 15 excluded

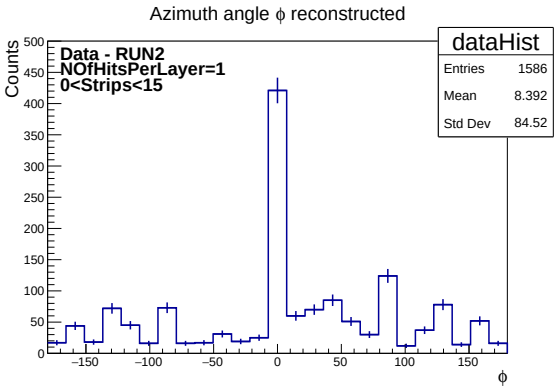

(c) Azimuth angle with strip 0 and 15 excluded

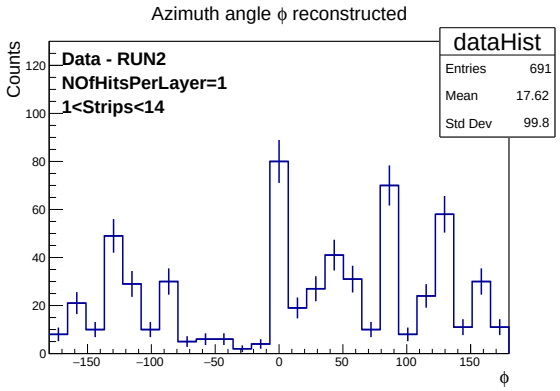

(d) Azimuth angle with strip 0, 1, 14 and 15 excluded

Figure 4: Angles reconstructed with cut : Number of hits per chamber equal to 1

Appendix .4: Simulation - additional plots

Appendix .4.1: Misalignment

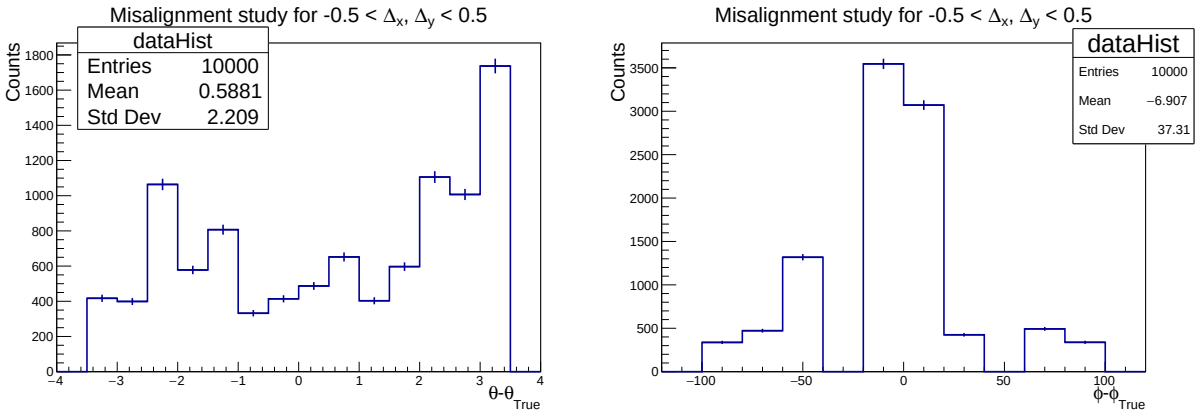

(a) Bias in zenith angle

(b) Bias in azimuth angle

Figure 5: Bias introduced due to misalignment of detectors for $-0.5cm < \Delta_x, \Delta_y < 0.5cm$

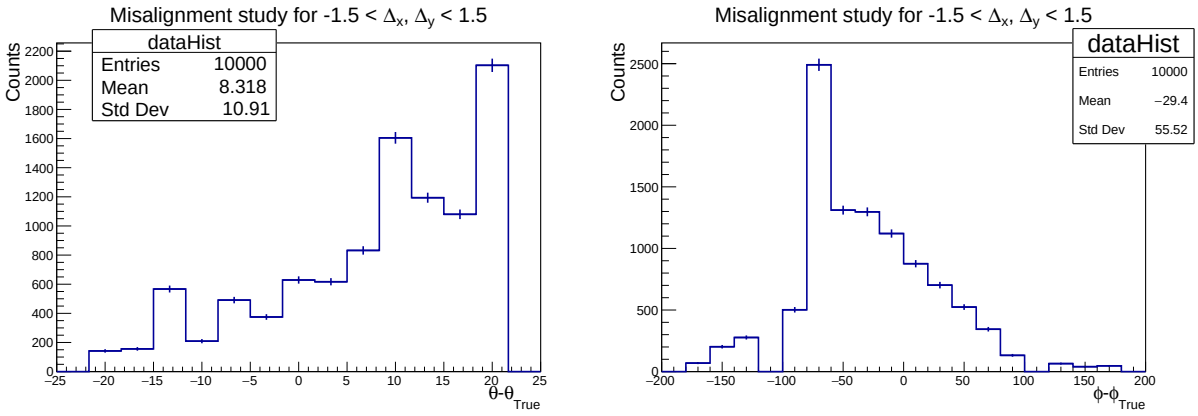

(a) Bias in zenith angle

(b) Bias in azimuth angle

Figure 6: Bias introduced due to misalignment of detectors for $-1.5cm < \Delta_x, \Delta_y < 1.5cm$

Appendix .4.2: Signal Induced for 1-mm gap

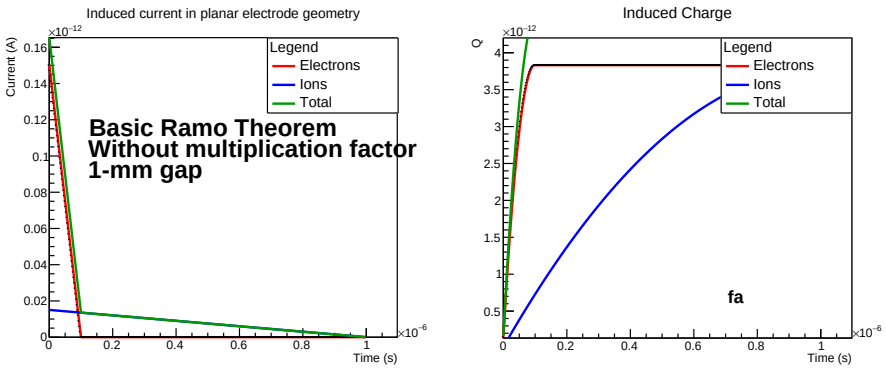

(a) Signal induced without multiplication factor

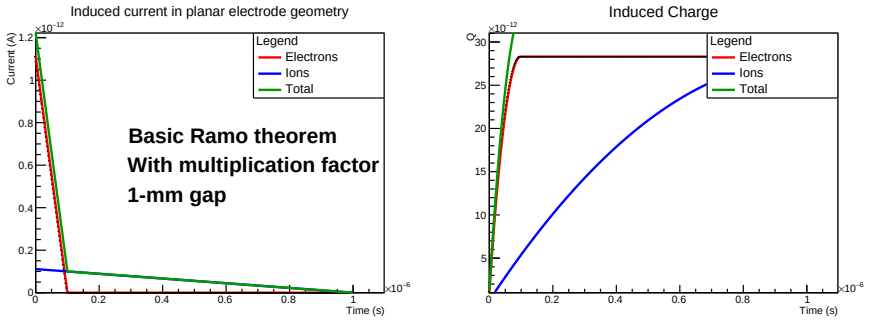

(b) Signal induced with multiplication factor

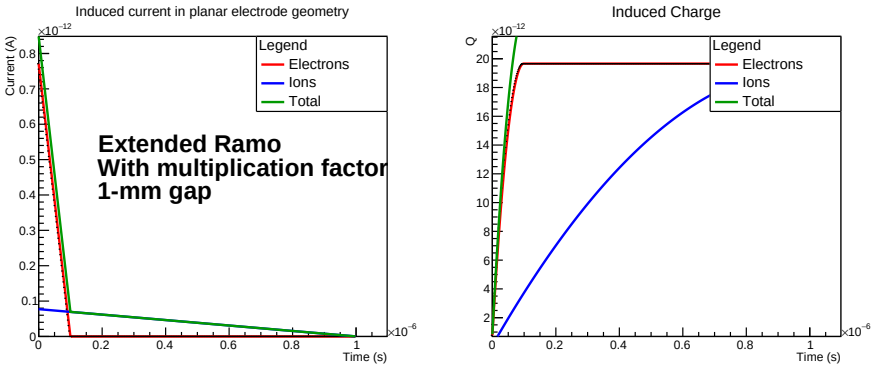

(c) Signal induced with multiplication factor - Extended Ramo theorem

Figure 7: Comparison of signals induced in parallel plate geometry of 1-mm gap according to Shockley-Ramo theorem (non)-extended